

Material Matters™

VOLUME 13 • NUMBER 2

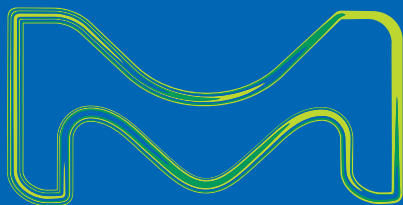
Atomic Layer Deposition Nanostructuring with ALD

NANOCOMPOSITE COATINGS with
Tunable Properties Prepared by
Atomic Layer Deposition

SILICON NITRIDE ATOMIC LAYER
DEPOSITION: A Brief Review of Precursor
Chemistry

GROUP 11 THIN FILMS by
Atomic Layer Deposition

FEW MONOLAYER ATOMIC LAYER DEPOSITION
on Surfaces and Interfaces for Energy Applications



Introduction



Taryn L. Fuhrman-Hall, M.B.A.

Product Manager,
Materials Science

Welcome to the second *Material Matters*™ issue of 2018. This issue explores atomic layer deposition (ALD) and the many disciplines in which it is utilized. The ALD process generates highly specific films with applications in many disciplines such as microelectronics, optics, sensors, solid-state detectors, battery and energy, nanomaterial growth, and solar power. The precision in which each layer can be deposited continues to make this a preferred process for advanced materials generation.

In the first article, Drs. Jeffrey Elam and Anil Mane (Argonne National Labs, USA) highlight the tunability of nanocomposite coatings and the remarkable suitability of atomic layer deposition for generating fit-for-purpose films. They specifically investigate the ALD mechanism of Mo:Al₂O₃ and W:Al₂O₃ films. They explore three specific practical applications of this technology for potential use in large-area photodetectors, electro-optical microsystems, and in concentrated solar power.

Silicon nitride is an essential material for semiconductor devices, and large-scale production of devices requires deposition of SiN at low temperatures. In the second article, Professor Jiyoung Kim (University of Texas at Dallas, USA) reviews currently available silicon precursor classes: silanes, chlorosilanes, organosilanes, and heterosilanes. The relative film properties and growth characteristics for each class of precursor is discussed, with emphasis on new and up-and-coming chemistry.

The third article from Professor Sean Barry (Carleton University, Canada) reviews the accessibility of the three coinage metals: copper, silver, and gold. He reviews how the availability of precursors to deposit metal films is predicted by their standard potentials. The author discusses the well-known field of copper deposition, but also highlights the rapidly emerging area of silver and gold deposition.

Atomically precise modification of surfaces and interfaces with few monolayer material leads to significant enhancements in properties, performance and reliability of heterogeneous materials and devices. In the fourth article, Professor Parag Banerjee (Washington University, USA) highlights the impact of insulators based on a few monolayers and wide bandgap semiconductors and metals deposited using atomic layer deposition (ALD). These materials are used to boost the performance of photovoltaics, batteries and catalysts.

Each article in this publication is accompanied by a list of relevant materials available from MilliporeSigma Materials Science. For additional product information, visit us at **SigmaAldrich.com/matsci**. As always, please bother us with your new product suggestions as well as thoughts and comments for *Material Matters*™ at **matsi@sial.com**.

About the Cover

Atomic layer deposition (ALD) uses alternating cycles of gaseous precursors to deposit materials onto a solid surface in an atomic layer-by-layer fashion. Our cover presents a literal and clear depiction of this layering effect in which the different color spheres represent the atoms of two distinct materials being layered onto a surface.

Merck KGaA
Frankfurter Strasse 250
64293 Darmstadt, Germany
Phone +49 6151 72 0

To Place Orders / Customer Service

Contact your local office or visit
SigmaAldrich.com/order

Technical Service

Contact your local office or visit
SigmaAldrich.com/techinfo

General Correspondence

Materials Science
materialsscience@sial.com

Subscriptions

Request your FREE subscription to *Material Matters*™ at **SigmaAldrich.com/mm**

The entire *Material Matters*™ archive is available at **SigmaAldrich.com/mm**

Material Matters™ (ISSN 1933-9631) is a publication of Merck KGaA.

Copyright (c) 2018 Merck KGaA, Darmstadt, Germany and/or its affiliates. All rights reserved. Merck, the vibrant M, Material Matters, and Sigma-Aldrich are trademarks of Merck KGaA, Darmstadt, Germany or its affiliates. All other trademarks are the property of their respective owners. Detailed information on trademarks is available via publicly accessible resources. More information on our branded products and services on **MerckMillipore.com**

Table of Contents

Articles

Nanocomposite Coatings with Tunable Properties Prepared by Atomic Layer Deposition	45
Silicon Nitride Atomic Layer Deposition: A Brief Review of Precursor Chemistry	55
Group 11 Thin Films by Atomic Layer Deposition	60
Few Monolayer Atomic Layer Deposition on Surfaces and Interfaces for Energy Applications	65

Featured Products

Precursors Packaged for Deposition Systems A selection of available ALD materials	53
Sputtering Targets A list of targets	54
Silicon Precursors A selection of ALD and solution deposition materials	57
Group 11 Deposition Materials A list of copper, silver and gold deposition materials	64
Titania Materials for Support and Solar Cells A list of titania nanomaterials and precursors	70
Lithium Precursors for Energy A selection of lithium precursors	70
Zinc Precursors for Catalysis A selection of zinc precursors	71



Bryce P. Nelson

Bryce P. Nelson, Ph.D.
Materials Science Initiative Lead

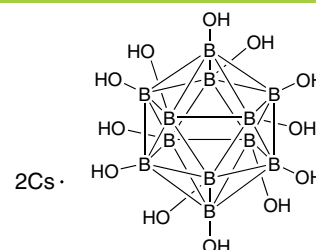
Dr. Alexander Spokoyny of the University of California — Los Angeles (USA) recommended the addition of cesium dodecahydroxydodecaborate (**902209**) to our catalog. This material represents a unique example of a robust inorganic polyol that can be used for the synthesis of well-defined small molecules, macromolecules and extended solid materials. It is conveniently synthesized and isolated as a Cs⁺ salt from a reaction between B₁₂H₁₂²⁻ precursor and 30% H₂O₂.¹⁻³ Recently, B₁₂(OH)₁₂²⁻ has been used for the synthesis of weakly-coordinating photoredox active reagents capable of initiating olefin polymerization.⁴ The stability of this cluster also allows the synthesis of atomically-precise nanomaterials capable of multivalent binding to protein surfaces⁵ as well as extending solids featuring unique photochemical and electronic properties.⁶⁻⁷

References

- (1) Peymann, T.; Knobler, C. B.; Khan, S. I.; Hawthorne, M. F. *J. Am. Chem. Soc.* **2001**, *123*, 2182–2185.
- (2) Bayer, M. J.; Hawthorne, M. F. *Inorg. Chem.* **2004**, *43*, 2018–2020.
- (3) Wixtrom, A. I.; Shao, Y.; Jung, D.; Machan, C. W.; Kevork, S. N.; Qian, E. A.; Khan, S. I.; Kubiak, C. P.; Spokoyny, A. M. *Inorg. Chem. Front.* **2016**, *3*, 711–717.
- (4) Messina, M. S.; Axtell, J. C.; Wang, Y.; Chong, P.; Wixtrom, A. I.; Kirlikovali, K. O.; Upton, B. M.; Hunter, B. M.; Shafaat, O. S.; Khan, S. I.; Winkler, J. R.; Gray, H. B.; Alexandrova, A. N.; Maynard, H. D.; Spokoyny, A. M. *J. Am. Chem. Soc.* **2016**, *138*, 6952–6955.
- (5) Qian, E. Q.; Wixtrom, A. I.; Axtell, J. C.; Saebi, A.; Rehak, P.; Han, Y.; Mouilly, E. H.; Mosallaei, D.; Chow, S.; Messina, M.; Wang, J.-Y.; Royappa, A. T.; Rheingold, A. L.; Maynard, H. D.; Kral, P.; Spokoyny, A. M. *Nature Chem.* **2017**, *9*, 333–340.
- (6) Jung, D.; Saleh, L. M. A.; Berkson, Z.; El-Kady, M. F.; Hwang, J. Y.; Mohamed, N.; Wixtrom, A. I.; Titarenko, E.; Shao, Y.; McCarthy, K.; Guo, J.; Martini, I. B.; Kraemer, S.; Wegener, E. C.; Saint-Criq, P.; Ruehle, B.; Langeslay, R. R.; Delferro, M.; Brosmer, J. L.; Hendon, C. H.; Gallagher-Jones, M.; Rodriguez, J.; Chapman, K. W.; Miller, J. T.; Duan, X.; Kaner, R. B.; Zink, J. I.; Chmelka, B. F.; Spokoyny, A. M. *Nat. Mater.* **2018**, *17*, 341–348.
- (7) Axtell, J. C.; Saleh, L. M. A.; Qian, E. A.; Wixtrom, A. I.; Spokoyny, A. M. *Inorg. Chem.* **2018**, *57*, 2333–2350.

Cesium dodecahydroxydodecaborate

[12589-26-3] B₁₂H₁₂O₁₂·2Cs



Boric acid (H₃B₃O₆), dicesium salt; Dodecaborate(2-), dodecahydroxy-, dicesium (9CI); Dicesium dodecahydroxy-closo-dodecaborate; Dicesium dodecahydroxydodecaborate(2-).

Store at 2-8°C

1g

902209-1G

Beyond pure

Ultra-high purity metals, salts, and oxides are essential in creating advanced materials. Explore the breadth of our portfolio's materials with purity of 99.999% or higher for applications such as:

- Photovoltaics
- Phosphor materials
- Nanoparticle synthesis
- Magnetic memory
- Biomedical applications
- Electronic devices



Product Description	Cat. No.
Metals	
Aluminum, wire, diam. 1.0 mm, 99.999% trace metals basis	266558
Antimony, beads, 1-5 mm, low oxide, 99.999% trace metals basis	452343
Bismuth, pieces, 1-12 mm, 99.999% trace metals basis	556130
Copper, powder, 99.999% trace metals basis	203122
Gallium, 99.9995% trace metals basis	203319
Germanium, chips, 99.999% trace metals basis	203343
Gold, beads, 1-6 mm, 99.999% trace metals basis	326542
Indium, beads, diam. 2-5 mm, 99.999% trace metals basis	264113
Selenium, pellets, <5 mm particle size, ≥99.999% trace metals basis	204307
Silicon, powder, -60 mesh, 99.999% trace metals basis	267414
Zinc, foil, thickness 0.25 mm, 99.999% trace metals basis	267619
Oxides	
Bismuth(III) oxide, powder, 99.999% trace metals basis	202827
Copper(II) oxide, 99.999% trace metals basis	203130
Europium(III) oxide, 99.999% trace metals basis	323543
Germanium(IV) oxide, powder, 99.999% trace metals basis	483001
Holmium(III) oxide, powder, 99.999% trace metals basis	229679
Iron(III) oxide, ≥99.995% trace metals basis	529311
Lanthanum(III) oxide, 99.999% trace metals basis	203556
Lead(II) oxide, 99.999% trace metals basis	203610
Mercury(II) oxide, 99.999% trace metals basis	203793
Zinc oxide, 99.999% trace metals basis	204951

Product Description	Cat. No.
Salts	
Aluminum chloride, anhydrous, powder, 99.999% trace metals basis	563919
Ammonium acetate, 99.999% trace metals basis	372331
Barium chloride dihydrate, ≥99.999% trace metals basis	529591
Cesium chloride, ≥99.999% trace metals basis	203025
Copper(I) bromide, 99.999% trace metals basis	254185
Copper(II) nitrate hydrate, 99.999% trace metals basis	229636
Gallium(III) chloride, beads, anhydrous, ≥99.999% trace metals basis	427128
Gold(III) chloride hydrate, 99.995% trace metals basis	254169
Indium(III) chloride, 99.999% trace metals basis	203440
Lanthanum(III) nitrate hexahydrate, 99.999% trace metals basis	203548
Lead(II) bromide, 99.999% trace metals basis	398853
Lead(II) iodide, beads, -10 mesh, 99.999% trace metals basis	554359
Silver nitrate, 99.9999% trace metals basis	204390
Sodium chloride, 99.999% trace metals basis	204439
Sodium nitrite, 99.999% trace metals basis	563218
Zinc nitrate hydrate, 99.999% trace metals basis	230006

For a complete list of ultra-high purity products, visit SigmaAldrich.com/uhp

Nanocomposite Coatings with Tunable Properties Prepared by Atomic Layer Deposition



Anil U. Mane and Jeffrey W. Elam*

Argonne National Laboratory, Argonne, Illinois 60439, USA
*Email: jelam@anl.gov

Introduction

Nanocomposite coatings, comprised of a precisely blended mixture of components, have diverse applications in microelectronics, optics, sensors, and solid-state detectors. By varying the composition of the mixture, the electrical, optical, and physical properties of the coatings can be “tuned” over almost the full range of the individual components, and can sometimes yield properties distinct from those of any of the constituents. There are many techniques for producing nanocomposite coatings, but atomic layer deposition (ALD) is particularly well suited for controlling the properties of the fabricated coatings. ALD uses alternating cycles of gaseous precursors to a solid surface to deposit materials in an atomic layer-by-layer fashion.¹ Because a chemical reaction on the surface naturally terminates when the surface functional groups are all reacted, the amount of material deposited in one ALD cycle is easily controlled. This self-limiting property, coupled with facile diffusion of the precursor vapors into narrow pores and voids, allows complex, 3-dimensional substrates to be coated with excellent uniformity and conformality.² ALD can be used to deposit a wide variety of materials including metal oxides, nitrides, sulfides, and even pure elements. By alternating between two materials (e.g., a metal and a metal oxide), we can synthesize complex nanocomposite coatings.^{3–5} The thickness of the coating is controlled by the total number of ALD cycles performed, and the composition is controlled by the ratio of the ALD cycles executed for each of the two components.

In this study, we employed *in situ* quartz crystal microbalance (QCM) measurements and Fourier transform infrared (FTIR) absorption spectroscopy to investigate the ALD growth mechanism of nanocomposite films comprised of Mo:Al₂O₃ and W:Al₂O₃. These films were prepared using alternating exposures to trimethyl aluminum (TMA) and H₂O for the Al₂O₃ ALD, and

alternating MF₆/Si₂H₆ exposures for the metal ALD, where M=Mo or W. In the case of the Mo:Al₂O₃ films, QCM showed that the Mo ALD inhibits the Al₂O₃ ALD and vice versa. Despite this inhibition, the relationship between Mo content and Mo cycle percentage was easily controlled. Surprisingly, FTIR revealed that the reducing agent for the Mo was not the Si₂H₆, but rather the TMA exposure from the subsequent Al₂O₃ ALD cycle. Elemental analysis showed that the M:Al₂O₃ films were uniform in composition and contained Al, O, and metallic Mo or W as expected, but also included significant F and C. Cross-sectional transmission electron microscopy revealed the film structure to be metallic nanoparticles (~1 nm) embedded in an amorphous matrix.

Three distinct practical applications of this technology are explored in this paper. We utilized these nanocomposite coatings to functionalize capillary glass array plates to fabricate large-area microchannel plates (MCPs) suitable for application in large-area photodetectors. In addition, we applied these films as charge drain coatings in electron-optical microsystems for a prototype electron beam lithography tool, permitting high-resolution electron beam patterns without charging artifacts. Finally, we explored the suitability of these films for use as selective solar absorbing coatings in concentrated solar power.

Experimental

Deposition of the Mo:Al₂O₃ and W:Al₂O₃ composite ALD film was performed at 200 °C in a hot-walled viscous flow ALD reactor.⁶ This reactor was equipped with a quartz crystal microbalance (QCM) that allowed *in situ* studies of the ALD processes. The TMA (97%, Sigma-Aldrich), deionized H₂O, Si₂H₆ (99.998%, Sigma-Aldrich), MoF₆ (99%, Alfa Aesar), and WF₆ (99.8%, Sigma-Aldrich) precursors were maintained at room temperature. The

ultrahigh purity (99.999%) N_2 carrier gas flow was set to 300 sccm, which provided a base pressure of 1.0 Torr in the ALD reaction chamber as measured by a heated Baratron pressure gauge (MKS model 629B). The $Mo:Al_2O_3$ and $W:Al_2O_3$ composite films were deposited on n -type Si(100) substrates. Prior to ALD, the substrates were cleaned using a 10 min ultrasonic treatment in acetone. For the Al_2O_3 ALD, TMA and H_2O were alternately pulsed into the N_2 carrier flow with the following sequence: 1s TMA dose (0.2 Torr) – 5s purge – 1s H_2O dose (0.3 Torr) – 5s purge. Similarly, the Mo and W ALD used alternating exposures to MoF_6/Si_2H_6 and WF_6/Si_2H_6 , respectively, with the timing sequence: 1s Si_2H_6 dose (0.25 Torr) – 5s purge – 1s MoF_6 or WF_6 dose (0.05 Torr) – 5s purge. These conditions for the Al_2O_3 , Mo, and W ALD provided self-limiting growth as verified by *in situ* QCM measurements.

In situ QCM was performed to examine the $Mo:Al_2O_3$ and $W:Al_2O_3$ composite ALD using different ALD pulse sequences. The QCM measurements typically used 10s N_2 purge times to allow the QCM signal to stabilize after each precursor exposure. Transmission electron microscopy (TEM) analysis was performed by Evans Analytical Group (Sunnyvale, CA). TEM samples were prepared using the *in situ* focussed ion beam (FIB) lift out technique on an FEI Strata Dual Beam FIB/SEM. The samples were capped with a protective layer of carbon prior to FIB milling, and were imaged with a FEI Tecnai TF-20 FEG/TEM operated at 200 kV in bright-field (BF) TEM mode, high-resolution (HR) TEM mode, and nanobeam diffraction (NBD) mode. The composition of the $Mo:Al_2O_3$ and $W:Al_2O_3$ composite layers was determined by depth profiling using X-ray photoelectron spectroscopy (XPS, Evans Analytical Group) and Rutherford backscattering spectroscopy (RBS, Evans Analytical Group). The metal content in the composite films was measured using X-ray fluorescence (XRF, Oxford ED2000).

The resistance of the $Mo:Al_2O_3$ and $W:Al_2O_3$ composite layers was determined by performing current-voltage (I-V) measurements using a Keithley Model 6487 current-voltage source. To facilitate I-V measurements on these highly resistive coatings, the films were deposited on insulating substrates with lithographically patterned comb structures comprised of interdigitated Au electrodes with a 2 μm spacing.⁷ These comb structures provided an 80,000 times greater effective contact area, and an equivalent boost in current compared to conventional four-point probe measurements. Additional I-V and electron amplification measurements were performed on $W:Al_2O_3$ layers deposited on high aspect ratio (60:1) borosilicate glass capillary arrays with 20 μm pores fabricated by Incom, Inc. (Charlton, MA). These capillary arrays were also coated with an eight nm ALD MgO emissive layer to boost the secondary electron coefficient, and both sides were coated with 100 nm evaporated nickel-chromium to provide a low resistance electrical contact.

In situ Fourier transform infrared (FTIR) measurements were performed during the $Mo:Al_2O_3$ ALD using a Nicolet 6700 with a liquid nitrogen-cooled MCT-B detector. For these measurements, the FTIR beam was diverted through CsI windows and into the

ALD reactor. The windows were protected by gate valves, which were closed during the ALD exposures to prevent deposition on the windows. The FTIR beam was directed through a sample comprised of ZrO_2 nanopowder pressed into a stainless steel grid to enhance the sample surface area and boost the optical absorption.⁸ Prior to the $Mo:Al_2O_3$ ALD, the ZrO_2 powder was coated using 10 cycles of TMA and H_2O for Al_2O_3 ALD.

Results and Discussion

Growth and Properties of $Mo:Al_2O_3$ Composite Films

Figure 1 shows a schematic of the precursor dosing strategy used to synthesize the $Mo:Al_2O_3$ ALD composite films. Alternating TMA/ H_2O exposures were used to deposit Al_2O_3 , and periodically a single MoF_6/Si_2H_6 cycle was performed to introduce the Mo. We define the Mo cycle percentage as: $\%Mo = Mo / (Mo + Al_2O_3) \times 100$ where Mo and Al_2O_3 are the relative numbers of TMA/ H_2O and MoF_6/Si_2H_6 cycles performed, respectively. Because of the drastically different resistivity for these two materials ($\sim 10^{16}$ and 10^{-4} Ohm cm for Al_2O_3 and Mo, respectively), we expected to be able to tune the resistivity for the composite film over a broad range by adjusting the Mo cycle percentage.

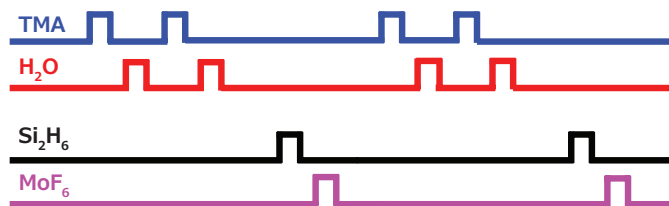


Figure 1. Schematic illustration of precursor pulsing sequence for ALD of $Mo:Al_2O_3$ nanocomposite coating using alternating TMA/ H_2O exposures for the Al_2O_3 ALD and alternating MoF_6/Si_2H_6 exposures for the Mo ALD.

Figure 2A shows *in situ* QCM measurements performed during the ALD of a $Mo:Al_2O_3$ composite film using a 10% Mo cycle percentage (nine Al_2O_3 ALD cycles followed by one Mo ALD cycle). The overall pattern consists of nine small mass gains followed by a single, larger mass gain, and this pattern is repeated three times. Figure 2B shows an expanded view of the boxed region in Figure 2A and reveals some informative details about the QCM mass gains. Between 95–115s, two TMA/ H_2O cycles for Al_2O_3 ALD are shown and the QCM signals match the expected pattern for Al_2O_3 ALD.³ The net mass gain for each Al_2O_3 ALD cycle is ~ 30 ng/cm², which is slightly smaller than the expected value. In contrast, the QCM signals observed during the MoF_6/Si_2H_6 exposures do not follow the pattern reported in the literature for Mo ALD.⁹ In particular, no mass gain is observed during the Si_2H_6 exposure, and the net mass gain is only ~ 250 ng/cm², which is far below the 1,000 ng/cm² expected for Mo ALD. It is interesting to note that the first TMA exposure following the Mo ALD cycle yields a sharp mass rise followed by a slow decay. This is the signature pattern for a temperature-induced QCM transient produced by an exothermic reaction.¹⁰

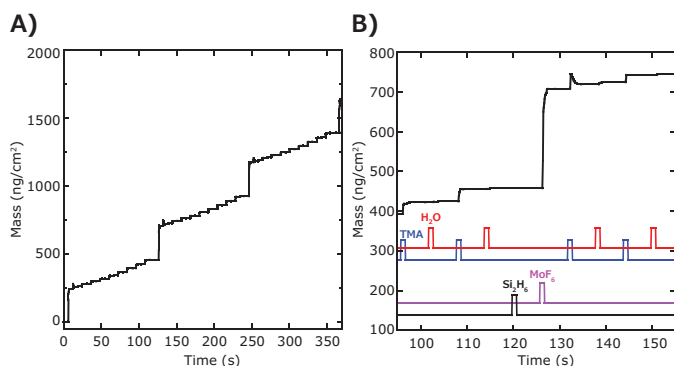


Figure 2. *In situ* QCM measurements during Mo:Al₂O₃ composite film ALD using a 10% Mo cycle percentage (nine Al₂O₃ ALD cycles followed by one Mo ALD cycle). **A)** Mass vs. time over 30 ALD cycles. **B)** Expanded view of the inset in **A**, with TMA, H₂O, Si₂H₆, and MoF₆ dose times are indicated.

Figure 3 shows the net mass gains following each ALD cycle for Mo (triangles) and Al₂O₃ (circles). The dashed, horizontal line shows the expected, steady-state mass gains for Al₂O₃ ALD at ~35 ng/cm². This figure illustrates that the Al₂O₃ ALD is inhibited by ~50% initially following the Mo ALD, and does not quite achieve the steady-state value even after nine Al₂O₃ ALD cycles. Moreover, the Mo ALD is also severely inhibited on the Al₂O₃ surface by ~75%.

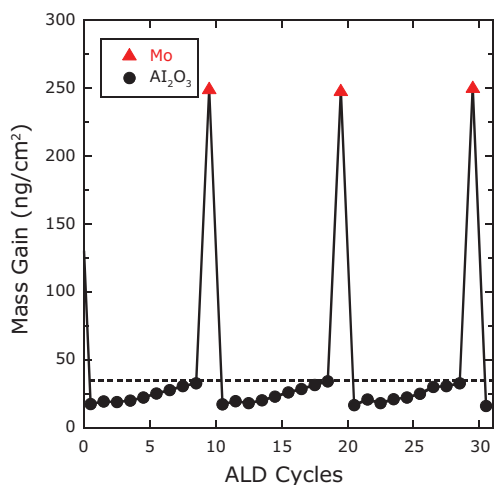


Figure 3. Net mass gains following each ALD cycle of Mo:Al₂O₃ composite film deposition using a 10% Mo cycle percentage. Mo and Al₂O₃ ALD cycles are indicated by the triangles and circles, respectively. The dashed, horizontal line shows the expected steady-state mass gain of 35 ng/cm² for Al₂O₃ ALD.

The origin for some of the unusual QCM results can be gleaned from the *in situ* FTIR measurements. Figure 4 shows the IR absorbance at 4000 cm⁻¹, measured following the individual precursor exposures, where the precursor pulsed immediately prior to recording the IR spectrum is indicated above each data point. The 4000 cm⁻¹ frequency was selected because it falls in a spectral region where there are no peaks from any of the surface functional groups, and therefore serves as an indirect measure of the relative conductivity of the film.¹¹ The IR absorbance at 4000 cm⁻¹ remains relatively constant during the TMA and H₂O exposures for Al₂O₃ ALD. We might expect the IR absorbance to increase during the Si₂H₆ exposures for the Mo ALD since Si₂H₆ is believed to be the reducing agent for the Mo.⁹ However, this is clearly not the case, as there is practically no change in the IR absorbance during the Si₂H₆ exposures. Instead, the IR absorbance increases sharply during the TMA exposures that follow the MoF₆ exposures. This finding suggests that TMA is in fact the reducing agent, which is consistent with the exothermic transients seen in the QCM data during the TMA exposures following MoF₆ exposures (Figure 2B). Additional evidence for the reducing effect of TMA on the adsorbed MoF₆ was indicated by a decrease in the MoOF_x stretching frequency at 1040 cm⁻¹ during the TMA exposures (spectra not shown).

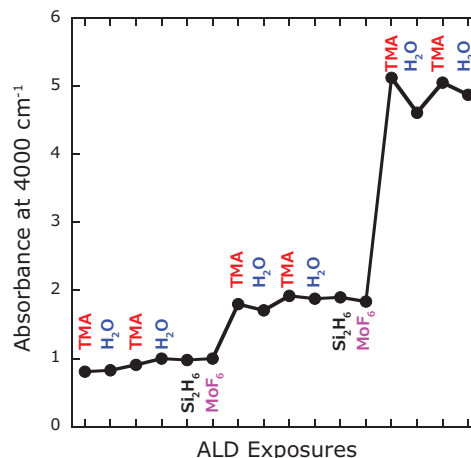


Figure 4. IR absorbance at 4000 cm⁻¹ measured by *in situ* FTIR following individual precursor exposures for the Mo:Al₂O₃ composite film ALD. The precursor pulsed immediately prior to recording the IR spectrum is indicated above each data point.

Figure 5 shows a low-resolution cross-sectional TEM image of a 40 nm Mo:Al₂O₃ composite film prepared on a Si(100) substrate using 10% Mo cycles. This film appears dense and continuous, and the top surface is relatively smooth and parallel to the Si substrate. The interface between the Si substrate and the Mo:Al₂O₃ composite film shows a low density, amorphous region attributed to the Si native oxide and Al₂O₃ from the initial ALD cycles. Under higher resolution (**Figure 5A**), the Mo:Al₂O₃ composite film is seen to consist of 1–2 nm particles (dark spots) embedded in a lower density matrix. Close inspection of the particles (**Figure 5A**, inset) reveals weak lattice fringes. Moreover, nano-beam diffraction measurements acquired from the nanocomposite film (**Figure 5B**) exhibit diffuse rings consistent with crystalline nanoparticles. Based on these observations, and on our previous study of the W:Al₂O₃ composite film ALD,⁵ we hypothesize that the crystalline nanoparticles in **Figure 5A** are metallic Mo. These Mo nanoparticles might form through the sintering of Mo atoms upon reduction of MoOF_x surface species by the TMA. The role of TMA as a reducing agent is somewhat surprising, but we believe this to be true based on our FTIR results, and because the microstructure and properties of the Mo:Al₂O₃ composite films are practically identical when the Si₂H₆ exposures are not performed.

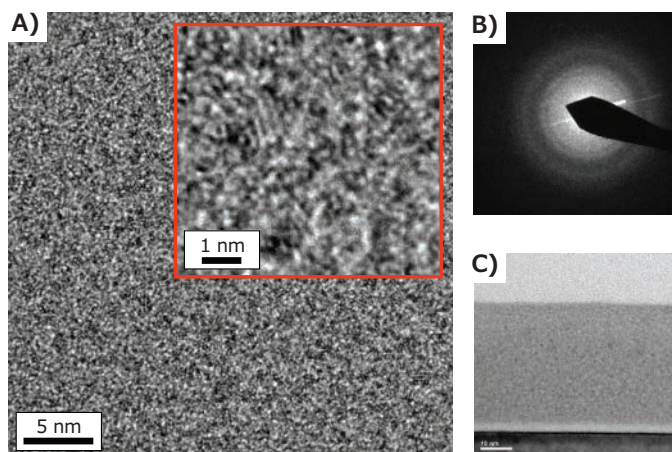


Figure 5. Cross-sectional TEM analysis of 40 nm Mo:Al₂O₃ composite film prepared on Si(100) substrate using 10% Mo cycles. **A)** High resolution image showing 1–2 nm particles (dark spots) embedded in a lower density matrix. **B)** Nano-beam diffraction of film region shown in **A**. **C)** Low resolution image of entire film thickness.

The composition of the Mo:Al₂O₃ composite films was determined using XPS depth profiling and RBS measurements of films prepared on Si(100) substrates. These measurements revealed that the films contained Al, O, and Mo as expected, but also contained ~5% C and ~10% F. XPS demonstrated that Mo exists in both the metallic and sub-oxide (Mo⁺⁴) states in the film. These findings, when combined with the QCM and FTIR measurements, suggest that the TMA reduces the adsorbed MoOF_x species to form AlF₃ and metallic Mo. In addition, the C and F presence in the films is similar to that in a previous study which concluded that alternating exposures to NbF₅ and TMA produced films comprised of NbF_x, NbC, C, and AlF₃.¹²

Next, a series of Mo:Al₂O₃ composite films was prepared on Si(100) substrates using different Mo cycle percentages and analyzed by X-ray fluorescence to determine the Mo content of the films. As shown in **Figure 6A**, the Mo content increases linearly from 2.1 to 9.0 mol% Mo as the Mo cycle percentage increases from eight to 15% Mo. This linear relationship demonstrates that the Mo content can be easily and precisely controlled by adjusting the Mo cycle percentage during the Mo:Al₂O₃ composite film ALD. The resistivity of the Mo:Al₂O₃ composite films was determined using current-voltage measurements of films deposited on comb structures, and the results are shown in **Figure 6B**. **Figure 6B** shows that the resistivity of the Mo:Al₂O₃ composite films can be tuned over a very broad range by adjusting the Mo cycle percentage. The range of resistivity values provided by these coatings (10⁴–10¹⁰ Ohm cm) is particularly useful for applications in electron multipliers and charge drain coatings, and this capability will be demonstrated below.

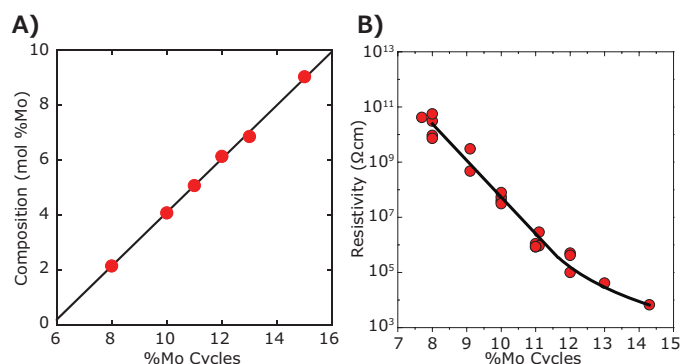


Figure 6. **A)** Mo content of ALD Mo:Al₂O₃ composite films as determined by XRF measurements versus Mo cycle percentage. **B)** Resistivity of ALD Mo:Al₂O₃ composite films as determined by current-voltage measurements versus Mo cycle percentage.

Growth and Properties of W:Al₂O₃ Composite Films

We performed *in situ* QCM measurements of the W:Al₂O₃ composite film grown by ALD to explore their growth behavior. We deposited and characterized a range of W:Al₂O₃ composite films while varying the W cycle percentage to determine the thickness, composition, morphology, and microstructure of these films and to establish the effect of W content on resistivity.⁵ Some of these results are presented in **Figure 7**.

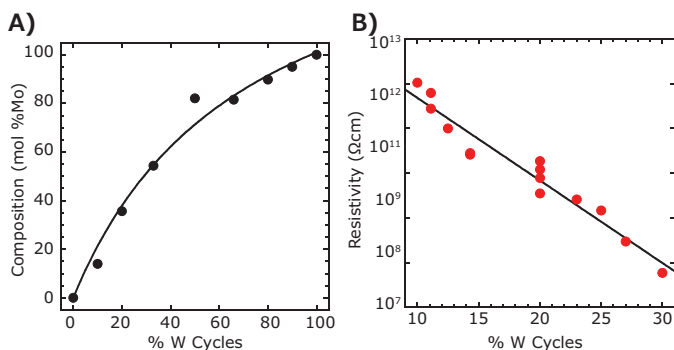


Figure 7. A) W content of ALD W:Al₂O₃ composite films deduced from *in situ* QCM versus W cycle percentage. B) Resistivity of ALD W:Al₂O₃ composite films determined by current-voltage measurements versus W cycle percentage.

Figure 7A shows the composition of the W:Al₂O₃ composite films as determined by *in situ* QCM versus W cycle percentage. The W mol% varies smoothly over the full range, and is approximately linear between 10–30%. **Figure 7B** shows the effect of varying the W cycle percentage on the resistivity as determined by current-voltage measurements of films deposited on comb chips and on capillary glass array substrates. The resistivity decreases approximately exponentially from $\sim 10^{12}$ Ohm cm at 10%W cycles to $\sim 10^8$ Ohm cm at 30% W cycles. This behavior is similar to that of the Mo:Al₂O₃ composite films (**Figure 6B**), although the slope is much steeper in the case of the Mo:Al₂O₃ composite films (6 decades over 4% change in Mo cycles) as compared to W:Al₂O₃ composite films (4 decades over 20% change in W cycles). This difference may stem from the much higher deposition rate for the Mo (~ 10 Å/cycle)⁹ versus the W (~ 4 Å/cycle)¹³ under similar growth conditions, especially in light of the exponential relationship between resistivity and metal content.

Next, we performed optical absorption measurements on the W:Al₂O₃ composite films prepared using 0–60% W cycles. The direct bandgaps were extracted from the absorption spectra using Tauc plots, and the results are shown in **Figure 8A**. The bandgap decreases with increasing W cycle percentage. **Figure 8B** shows the absorption coefficients as a function of photon energy for these coatings and clearly shows that the absorption onset shifts to lower energies with increasing W cycle percentages between 10–40%, and then transitions to a broadband, metallic absorption for the higher W cycle percentages of 50–60%. This tunable absorption property is desirable for selective solar absorption coatings that must absorb visible light while transmitting or reflecting infrared wavelengths, as discussed next.

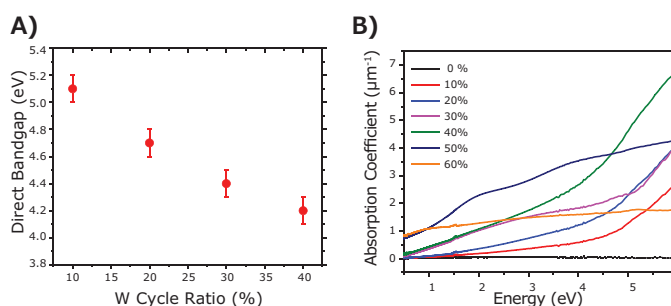


Figure 8. A) Direct bandgap versus W cycle percentage and B) absorption coefficient versus photon energy for ALD W:Al₂O₃ composite films prepared using 0–60% W cycle percentage.

Other Nanocomposite Coatings

Similar to the coating strategies previously described, we have developed ALD methods for nanocomposite coatings using combinations of W, Mo, Ta, Nb, and Co metals, and Al₂O₃, ZrO₂, HfO₂, MgO, and TiO₂ dielectrics. Although a complete description is beyond the scope of this article, we note that the trends of increasing electrical conductivity, decreasing bandgap, and increasing absorption coefficient with increasing metal content are common to all of these materials.

Applications for Tunable Resistance Coatings

Microchannel Plates (MCPs)

Microchannel plates (MCPs) are solid-state electron amplifiers comprised of a two-dimensional array of microscopic channels in the form of a thin, flat plate. MCPs are used in detectors to identify low levels of electrons, ions, photons, or neutrons, and provide an amplified response via gain from secondary electron emission that occurs within the individual channels of the MCP.¹⁴ This unique quality allows MCPs to form images, and is critical to a wide variety of detectors and devices. Conventional MCP fabrication involves using multi-fiber glass working techniques to draw and assemble an array of solid-core fibers into a block. The block is subsequently sliced into thin wafers, and the solid cores are chemically etched to form an ordered array of pores comprised of lead silicate glass. Hydrogen firing is then used to activate the channel walls for electron multiplication. One drawback of this process is that the electrical conductivity and the secondary electron emission properties of the MCP cannot be adjusted independently, because both of these properties are imparted during the hydrogen-firing step. An additional drawback is that the aspect ratio (pore length to pore diameter) of the pores is limited to ~ 100 because the chemical etchant cannot diffuse into longer pores without dissolving the lead silicate cladding. This limits the gain that can be achieved.

An alternative strategy for MCP manufacturing is to functionalize glass capillary array wafers using ALD to impart the necessary conductivity and secondary emission properties.^{15,16} This process is illustrated in **Figure 9** for a 1.2 mm thick, 33 mm diameter disc with a pore size of 20 μm (**Figure 9A–C**). **Figure 9D** shows the 33 mm capillary array disc after ALD of a 94 nm Mo:Al₂O₃ composite film to serve as a resistive layer, and an 8 nm ALD MgO to enhance the secondary electron emission

of the surface.¹⁷ After the ALD, nickel-chromium electrodes were evaporated onto both sides of the disc to generate the MCP shown in **Figure 9E**. The ability to tune the resistivity of the ALD composite film allows MCPs to be manufactured over a broad resistance range so as to be optimized for specific detector applications.

The fully functionalized MCP shown in **Figure 9E** was evaluated in a high vacuum system equipped with a calibrated electron source and a phosphor screen to determine its gain and spatial uniformity. As shown by the photograph of the phosphor screen image in **Figure 9F**, the MCP response is uniform across the surface. Next, a pair of identical MCPs was assembled in series and installed in front of a position-sensitive anode. Using a photon counting mode and weak ultraviolet illumination, a two-dimensional map of the spatial distribution of the gain was generated (**Figure 9G**), again showing the uniformity of the gain across the MCP. Studies on the performance of ALD MCPs have also been reported.¹⁴

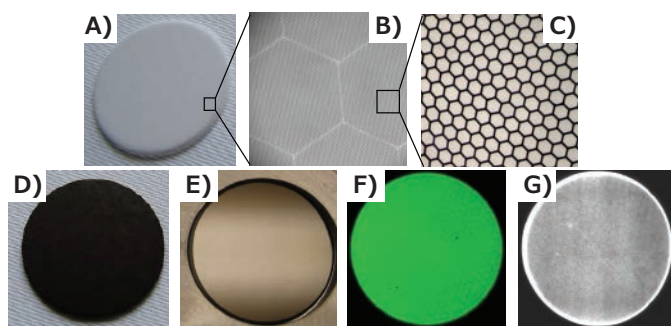


Figure 9. MCP fabrication using ALD tunable resistance coatings. **A-C)** Increasing resolution of 33 mm diameter borosilicate glass capillary array substrate comprised of hexagonal bundles of 20 μm pores. **D)** Glass substrate after 94 nm ALD $\text{Mo:Al}_2\text{O}_3$ composite resistive layer and eight nm ALD MgO emissive layer. **E)** Completed MCP with nickel-chromium electrodes. **F)** Phosphor screen illuminated with electrons amplified by ALD MCP. **G)** Gain map for pair of ALD MCPs.

One of the benefits of using ALD for MCP manufacturing is that it facilitates scaling to larger detector sizes. The dark circular disk in **Figure 10** is the 33 mm MCP described above. To the left of this small MCP is an 8 x 8" glass capillary array substrate in a metal transport case. To the right is an identical 8 x 8" plate after ALD functionalization and electrode deposition to produce a large-area MCP. This is the largest MCP ever produced. Work is underway in the Large Area Picosecond Photodetector Project led by Argonne National Laboratory to implement these MCPs for applications in high-energy physics.^{14,15}

Charge Drain Coatings

Electrostatic charging is a challenging problem in electron-optical devices such as mass spectrometers, particle detectors, and micro-electro mechanical systems (MEMS). When stray electrons strike the surfaces of insulating components in a vacuum environment, the electrons become trapped, creating an electrostatic charge. With no means of draining the accumulated

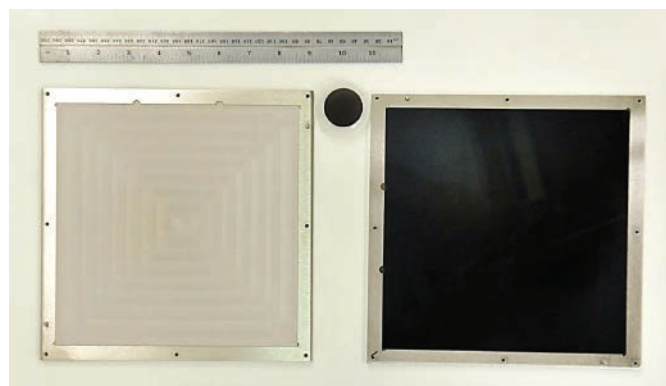


Figure 10. Uncoated 8 x 8" glass capillary substrate in metal transport case (left) next to identical, 8x8" glass substrate after ALD $\text{Mo:Al}_2\text{O}_3$ composite coating. Ruler and 33 mm MCP are shown for scale.

electrostatic charge, which can generate potentials of several kilovolts, the local electric fields become distorted causing loss of focus, resolution, and timing. Simple conducting or semiconducting films are unsuitable for draining this charge because the high leakage current can exceed the power supply or damage the device through resistive heating. Instead, a thin film with resistivity in the mesoscale (between those of a semiconductor and an insulator, 10^2 - 10^7 Ohm cm), is needed. In electron-optical MEMS, the challenge is aggravated by the much closer proximity of the electrons to the surfaces, and the films are subjected to very high electrical fields of up to 25 MV/m. Furthermore, the film must coat all surface orientations while maintaining nanoscale uniformity to ensure equivalent performance across all components.

The ALD tunable resistance nanocomposite films are an excellent candidate for charge drain coatings. We have demonstrated their benefit in the reflective electron beam lithography (REBL) Nanowriter — a high throughput, direct-writing, maskless lithography tool under development at KLA—Tencor.¹⁸ A schematic of the Nanowriter is shown in **Figure 11A**. The heart of the patterning system is the digital pattern generator (DPG) chip (**Figure 11B**). The DPG is an integrated circuit chip with an array of small, independently controllable electron mirrors ("lenslets") producing over 1 million "beamlets". The lenslet electrode MEMS structure is fabricated on top of complementary metal oxide semiconductor (CMOS) circuitry that provides voltage to four electrodes per lenslet to establish the electric fields required to produce an electrostatic lens for each pixel. The pixels and lenslets of the array are located on a 1.6 μm pitch, and the lenslet structure is \sim four μm in height. The DPG chip operates under a constant illumination of electrons, and this can lead to electrostatic charging on the insulating oxide surface along the wall of the lenslet (**Figure 11C**) that reduces the image quality (**Figure 12G**). To overcome this problem, a KLA-Tencor DPG chip was coated using an ALD $\text{Mo:Al}_2\text{O}_3$ composite coating to drain static charge (**Figure 11D**). **Figures 12A–F** show images of electron beam test patterns obtained using this DPG. These images indicate virtually defect-free DPG patterns.¹⁹

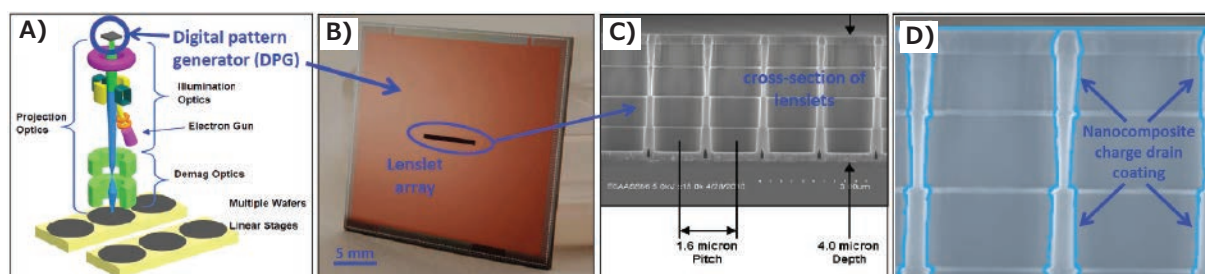


Figure 11. A) Schematic of KLA-Tencor REBL Nanowriter. B) REBL digital pattern generator (DPG). C) Cleaved cross-section of DPG MEMS lenslet array structure. D) Schematic of ALD charge drain coating covering DPG lenslet array.

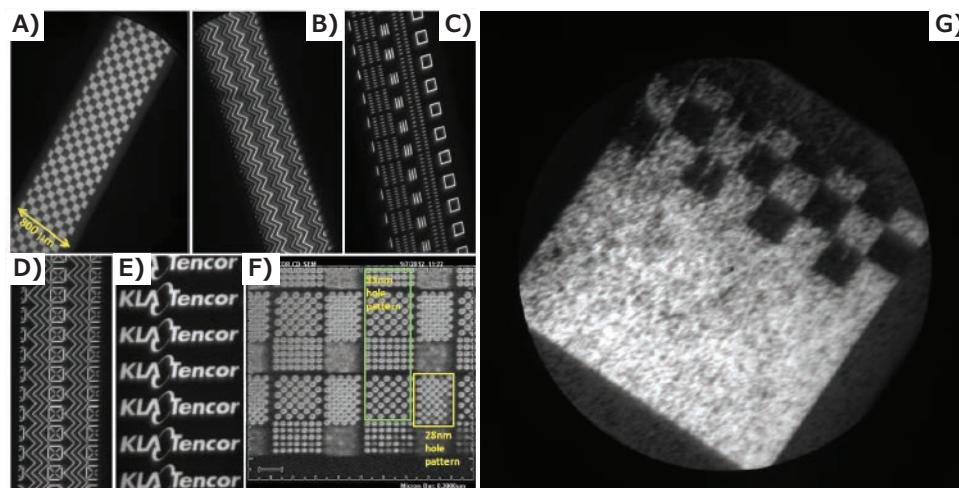


Figure 12. Defect-free test pattern images from DPG coated using ALD Mo:Al₂O₃ composite charge drain coating. A) Square pattern, B) chevron pattern, C) stitching pattern, D) stig test pattern, E) KLA-Tencor company logo, and F) contact hole pattern. G) Poor quality pattern from DPG without ALD Mo:Al₂O₃ charge drain coating.

Solar Selective Coatings

Concentrated solar thermal power combines both energy harvesting and energy storage in a single plant, making it very appealing. Solar “power tower” facilities can generate hundreds of megawatts using a vast array of mirrors to reflect solar radiation onto a central receiver, where the energy is absorbed and used to heat a fluid that can be stored, or used to drive a turbine for electric power (**Figure 13A**). The efficiency can be increased using a solar-selective coating that absorbs strongly in the visible solar spectrum, while simultaneously reflecting infrared (IR) wavelengths. A high IR reflectivity ensures that the receiver will not radiate IR energy at high operating temperatures, allowing more of the energy to be captured and used. In addition, the coating must endure high temperatures without losing its selective absorption properties.

As described above, the optical absorption of the ALD W:Al₂O₃ composite films can be tuned by adjusting the W content. This coating can be deposited on a metal substrate to absorb visible light while reflecting IR wavelengths. We prepared a 100 nm ALD W:Al₂O₃ composite film using 33% W cycle percentage on a Hayes 230 nickel superalloy coupon that had been pre-coated

with a high surface area mesoporous film. The resulting material is opaque in the visible, but highly reflective in the IR. **Figure 13B** shows the substrate after 12 hours in air at 800 °C, and 50 thermal shock cycles between 300–800 °C in air. Most conventional materials would oxidize during this treatment and become transparent, but our ALD nanocomposite coating is extremely stable at high temperatures in air, and remains black. Moreover, our coating resists cracking and delamination during repeated thermal cycling that simulates the day-night temperature changes. These ALD materials are very promising for use as selective solar absorbing coatings in next-generation concentrated solar thermal power facilities.

Conclusions

We have developed nanocomposite coatings built from conducting, metallic nanoparticles embedded in an amorphous dielectric matrix. These films are comprised of ALD M:D films where M= W, Mo, Ta, Nb or Co, and D= Al₂O₃, ZrO₂, HfO₂, MgO, or TiO₂. By varying the ratio of ALD cycles for metal and Al₂O₃ layers, we can tune precisely the resistance of these

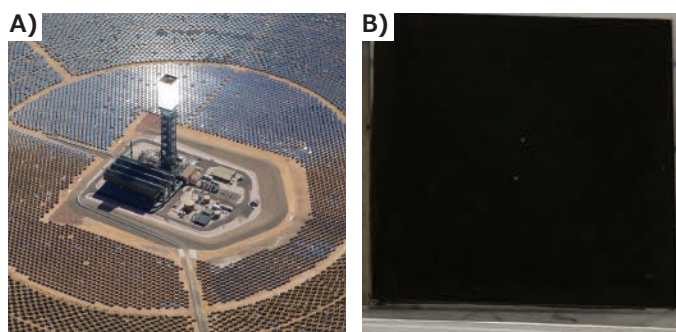


Figure 13. A) Aerial photograph of Ivanpah concentrated solar thermal power facility showing array of mirrors focussing sunlight on central receiving tower. B) 100nm ALD W:Al₂O₃ composite films prepared using 33% W cycle percentage on Hayes 230 nickel superalloy coupon that had been pre-coated with high surface area mesoporous film after 12 hours in air at 800 °C, and 50 thermal shock cycles between 300–800 °C in air.

coatings over a very broad range from 10^5 – 10^{12} Ohm cm, and the bandgap and absorption coefficient across the visible spectrum. We employed *in situ* QCM and FTIR absorption spectroscopy to understand the ALD growth mechanism for the Mo:Al₂O₃ nanocomposite films, showing that TMA serves as the reducing agent to form the conducting Mo. Cross-sectional TEM revealed the film structure to be metallic nanoparticles (1–2 nm) embedded in an amorphous matrix. We utilized these nanocomposite coatings to functionalize capillary glass array plates to fabricate large-area MCPs suitable for application in large-area photodetectors. In addition, we have applied these films as charge drain coatings in MEMS devices for a prototype electron beam lithography tool, and as selective solar absorbing coatings. These practical applications promise a bright future for the use of ALD for creation of nanocomposite coatings for specific commercial applications.

Acknowledgements

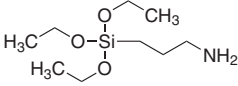
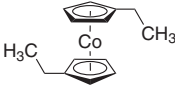
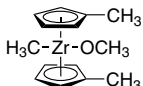

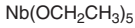

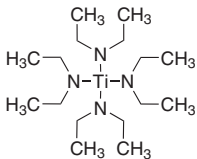
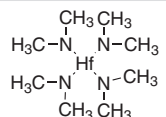
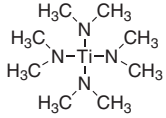
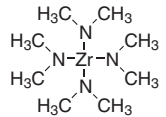
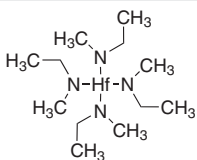
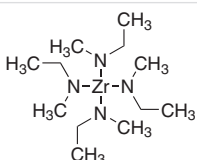
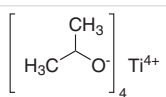

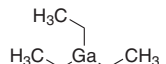
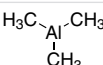
This work was supported by the U.S. Department of Energy, Office of Science, Office of Basic Energy Sciences and Office of High Energy Physics under contract DE-AC02-06CH11357 as part of the Large Area Picosecond Photodetector (LAPPD) project. The work at KLA-Tencor was partly sponsored by Defense Advanced Research Projects Agency under contract number HR0011-07-9-0007. The views, opinions, and/or findings contained in this article/presentation are those of the author/presenter and should not be interpreted as representing the official views or policies, either expressed or implied, of the Defense Advanced Research Projects Agency or the Department of Defense.

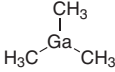
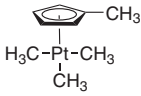
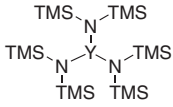
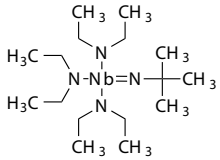
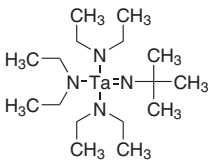
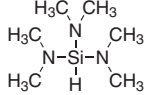
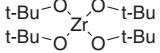
References

- (1) George, S. M. *Chem. Rev.* **2010**, *110*(1), 111–113.
- (2) Elam, J. Coatings on High Aspect Ratio Structures in *Atomic Layer Deposition of Nanostructured Materials*. Pinna, N. and Knez, M., Eds. Weinheim: Wiley-VCH. **2012**, 227.
- (3) Elam, J. W.; George, S. M. *Chem. Mater.* **2003**, *15*, 1020.
- (4) Elam, J. W.; Routkevitch, D.; George, S. M. *J. Electrochem. Soc.* **2003**, *150*, 6, G339.
- (5) Mane, A. U.; Elam, J. W. *Chem. Vap. Deposition* **2013**, *19*, 186.
- (6) Elam, J. W.; Groner, M. D.; George, S. M. *Rev. Sci. Instrum.* **2002**, *73*(8), 2981.
- (7) Brodie, A.; De Cecco, P.; Bevis, C.; Maldonado, J. R.; Bhatia, R.; Deguns, E.; Sundaram, G. Fabrication of Coatings with Targeted Tunable Electrical Properties via ALD: Al₂O₃/ZnO and Nb₂O₅/Ta₂O₅ in *Atomic Layer Deposition Applications 6*. Elam, J. W.; DeGendt, S.; VanDerStraten, O.; Delabie, A.; Londergan, A.; Bent, S. F.; Roozeboom, F.; Eds. **2010**, *33*, 101.
- (8) Ferguson, J. D.; Weimer, A. W.; George, S. M. *Appl. Surf. Sci.* **2000**, *180*, 162–163.
- (9) Seghete, D.; Rayner, Jr. G. B.; Cavanagh, A. S.; Anderson, V. R.; George, S. M. *Chem. Mater.* **2011**, *23*(7) 1668.
- (10) Christensen, S. T.; Elam, J. W. *Chem. Mater.* **2010**, *22*(8), 2517.
- (11) Du, X.; Du, Y.; George, S. M. *J. Phys. Chem. A*, **2008**, *112*(39) 9211.
- (12) Klug, J. A.; Proslie, T.; Elam, J. W.; Cook, R. E.; Hiller, J. M.; Claus, H.; Becker, N. G.; Pellin, M. J. *J. Phys. Chem. C*, **2011**, *115*(50) 25063.
- (13) Fabreguette, F. H.; Sechrist, Z. A.; Elam, J. W.; George, S. M. *Thin Solid Films* **2005**, *488*(1–2), 103.
- (14) Siegmund, O. H. W.; McPhate, J.; Tremsin, A. S.; Jelinsky, S. R.; Frisch, H. J.; Elam, J. W.; Mane, A. U.; Wagner, R. G.; Minot, M. J.; Renaud, J. M.; Detarando, M. A. *Phys. Procedia* **2012**, *37*, 803.
- (15) Mane, A. U.; Peng, Q.; Elam, J. W.; Bennis, D. C.; Craven, C. A.; Detarando, M. A.; Escolás, J. R.; Frisch, H. J.; Jokela, S. J.; McPhate, J.; Minot, M. J.; Siegmund, O. H. W.; Renaud, J. M.; Wagner, R. G.; Wetstein, M. J. An atomic layer deposition method to fabricate economical and robust large area microchannel plates for photodetectors, in *Proceedings of the 2nd International Conference on Technology and Instrumentation in Particle Physics*. Liu, T.; Ed. **2012**, *37*, 722.
- (16) D. R. Beaulieu, D. Gorelikov, H. Klotzsch, P. de Rouffignac, K. Saadatmand, K. Stenton, N. Sullivan, and A. S. Tremsin, *Nucl. Instrum. Methods Phys. Res. A* **2011**, *633*, S59.
- (17) Jokela, S. J.; Veryovkin, I. V.; Zinovev, A. V.; Elam, J. W.; Mane, A. U.; Peng, Q.; Insepov, Z.; et al. Secondary electron yield of emissive materials for large-area micro-channel plate detectors: surface composition and film thickness dependencies in *Proceedings of the 2nd International Conference on Technology and Instrumentation in Particle Physics*. Liu, T.; Ed. **2012**, *37*, 740.
- (18) Petric, P.; Bevis, C.; McCord, M.; Carroll, A.; Brodie, A.; Ummethala, U.; Grella, L.; Cheung, A.; Freed, R. J. *Vac. Sci. Technol. B* **2010**, *28*(6), C6C6.
- (19) Tong, W. M.; Brodie, A. D.; Mane, A. U.; Fuge, S.; Kidwingira, F.; McCord, M. A.; Bevis, C. F.; Elam, J. W. *Appl. Phys. Lett.* **2013**, *102*(25), 252901.

Precursors Packaged for Deposition Systems

For a complete list of available materials, visit SigmaAldrich.com/ald.

Name	Acronym	Structure	Form	Cat. No.
(3-Aminopropyl)triethoxysilane	APTES; APTS		liquid	706493-20ML
Bis(ethylcyclopentadienyl)cobalt(II)	(EtCp) ₂ Co		liquid	753076-10G
Bis(methyl-η ⁵ -cyclopentadienyl) methoxymethylzirconium	ZrD-CO ₄ ; ZRCMMM		liquid	725471-10G
Diethylzinc	DEZ; DEZn; Et ₂ Zn		liquid	668729-25G
Niobium(V) ethoxide	NbOEt		liquid	760412-10G
Silicon tetrachloride	STC		liquid	688509-25ML
Tetrakis(diethylamido)titanium(IV)	TDEAT		liquid	725536-10G
Tetrakis(dimethylamido)hafnium(IV)	TDMAH		low-melting solid	666610-25G
Tetrakis(dimethylamido)titanium(IV)	TDMAT		liquid	669008-25G
Tetrakis(dimethylamido)zirconium(IV)	TDMAZ		solid	669016-25G
Tetrakis(ethylmethylamido) hafnium(IV)	TEMAH		liquid	725544-10G
Tetrakis(ethylmethylamido) zirconium(IV)	TEMAZ		liquid	725528-10G
Titanium(IV) isopropoxide	TTIP		liquid	687502-25G
Titanium tetrachloride	TTC		liquid	697079-25G
Triethylgallium	TEG; TEGa; Et ₃ Ga		liquid	730726-10G
Trimethylaluminum	TMA		liquid	663301-25G

Name	Acronym	Structure	Form	Cat. No.
Trimethylgallium	TMG; TMGa; Me ₃ Ga		liquid	730734-10G
Trimethyl(methylcyclopentadienyl)platinum(IV)	MeCpPtMe ₃		low-melting solid	697540-10G
Tris[N,N-bis(trimethylsilyl)amide]yttrium	YDTMSA		powder	702021-10G
Tris(diethylamido)(tert-butylimido)niobium(V)	-		liquid	751774-10G
Tris(diethylamido)(tert-butylimido)tantalum(V)	TBTDET		liquid	668990-10G
Tris(dimethylamino)silane	TDMAS		liquid	759562-25G
Tungsten hexacarbonyl	-	W(CO) ₆	solid	755737-25G
Water	-	H ₂ O	liquid	697125-25ML
Zirconium(IV) tert-butoxide	ZTB		liquid	759554-25G

Sputtering Targets

For a complete list of available materials, visit [SigmaAldrich.com/sputtering-target](https://www.sigmaaldrich.com/sputtering-target).

Name	Structure	Purity (%) Or Grade	Cat. No.
Aluminum	Al	99.9995% trace metals basis, sputtering target	749036-1EA
Aluminum zinc oxide	Al ₂ O ₃ / ZnO	99.99% trace metals basis, sputtering target	752665-1EA
Chromium	Cr	99.95% trace metals basis, sputtering target	749052-1EA
Copper	Cu	99.95% trace metals basis, sputtering target	767476-1EA
Indium tin oxide	In ₂ O ₃ /SnO ₂	99.99% trace metals basis, sputtering target	752657-1EA
Nickel	Ni	99.95% trace metals basis, sputtering target	767484-1EA
Silicon	Si	99.999% trace metals basis, sputtering target	767492-1EA
Tantalum	Ta	99.95% trace metals basis, sputtering target	767514-1EA
Titanium	Ti	99.995% trace metals basis, sputtering target	749044-1EA
Tungsten	W	99.95% trace metals basis, sputtering target	767506-1EA
Yttrium(III) oxide	Y ₂ O ₃	99.99% trace metals basis, sputtering target	774022-1EA
Yttrium	Y	99.9% trace metals basis, sputtering target	773972-1EA
Zinc oxide	ZnO	99.99% trace metals basis, sputtering target	752681-1EA
Zinc	Zn	99.995% trace metals basis, sputtering target	749060-1EA
Zirconium(IV) oxide	ZrO ₂	99.95% trace metals basis (excludes 2% HfO ₂), sputtering target	774030-1EA
Zirconium(IV) oxide-yttria stabilized	ZrO ₂ / Y ₂ O ₃	99.9% trace metals basis, sputtering target	774049-1EA
Zirconium yttrium alloy	Zr _{0.85} Y _{0.15}	99.9% trace metals basis (excluding ≤1% Hf), sputtering target	774057-1EA

Silicon Nitride Atomic Layer Deposition: A Brief Review of Precursor Chemistry



Antonio T. Lucero, Jiyoung Kim*

Department of Materials Science and Engineering,
The University of Texas at Dallas, Richardson, TX 75080, USA
*Email: jiyoung.kim@utdallas.edu

Introduction

Silicon nitride (SiN_x) is a critical material for semiconductor devices, increasingly used in high-performance logic and memory. Modern, scaled devices require robust SiN films deposited at low temperature ($<400^\circ\text{C}$) for use as gate sidewall spacers and in self-aligned quadruple patterning.¹ Traditional SiN_x deposition techniques, including chemical vapor deposition (CVD) and plasma-enhanced chemical vapor deposition (PECVD), are now giving way to atomic layer deposition (ALD). ALD allows more control over the thickness of deposition, work at relatively low temperatures, and conforms over high-aspect ratio structures.² ALD can be divided into two classes, thermal ALD and plasma-enhanced ALD (PEALD). Both methods have some advantages for SiN_x deposition. Thermal ALD allows for conformal deposition over high aspect ratio (HAR) structures ($>5000:1$), while PEALD can be used at much lower temperatures with lower HAR conformality. Advances in precursor chemistry and nitrogen sources have enabled the tailoring of material properties like the wet etch rate and growth rate to meet research and industry requirements. There are currently three main silicon precursor classes: chlorosilanes, organosilanes, and heterosilanes. Chlorosilanes are silicon precursors where Si-Cl bonding is predominant. Organosilanes are silicon precursors containing organic ligands, although currently this class is limited to aminosilanes in practice. The last group, heterosilanes, includes all other precursors.

Chlorosilanes

Chlorosilanes are an historically important class of silicon precursors that helped to build the semiconductor industry by enabling the production of ultra-high purity silicon. This class includes any silicon precursor containing at least one chlorine-silicon bond. The first SiN_x was grown by thermal ALD in 1997, when Morishita³ deposited SiN_x using hexachlorodisilane (HCDS , Si_2Cl_6 , **Cat. No. 205184**) and hydrazine (N_2H_4 , **Cat. No. 215155**) at temperatures ranging from 525 – 650°C . While hydrazine has since been replaced by more convenient nitrogen sources, HCDS has remained an important precursor for SiN_x ALD. Later reports⁴ of ALD using HCDS and ammonia demonstrate successful deposition of SiN_x at temperatures as

low as 515 – 557°C . In addition, tetrachlorosilane,⁵ dichlorosilane (DCS),⁶ and octachlorotrisilane⁷ have all been used successfully. Since the deposition temperature is fairly high, the physical properties such as density and wet etch rate (WER) in hydrofluoric acid are good. Growth per cycle (GPC) varies, but is typically greater than 1 \AA/cycle . A disadvantage of chlorosilanes for thermal ALD of SiN_x is the large precursor exposure (10^7 – 10^{10} L) required to achieve saturation. Of note, only chlorosilane precursors have been used for thermal ALD of SiN_x , since they are the only precursors stable enough for use above 400°C , the temperature at which ammonia is activated. With the exception of hydrazine, which will be discussed in a later section, no other nitrogen sources are available for thermal ALD. This limitation has prevented the widespread industry adoption of thermal ALD for SiN_x growth.

In order to grow films at low ($<400^\circ\text{C}$) temperatures, research has focused on the use of plasma to aid deposition.⁸ Microwave plasma, inductively coupled plasma (ICP), and capacitively coupled plasma (CCP) are most commonly used in combination with sources of reactive nitrogen including ammonia, nitrogen, or nitrogen forming gas ($\text{N}_2\text{-H}_2$). DCS ⁹ and HCDS ¹⁰ have been used extensively with ammonia in PEALD of SiN_x at temperatures from 300 – 400°C . Temperatures less than 300°C can lead to excess chlorine contamination due to the formation of NH_4Cl . Ovanesyan et al.¹⁰ reported conformal deposition of SiN_x on HAR structures using HCDS and NH_3 plasma at 400°C , with hydrogen in the form of $-\text{NH}$ and chlorine ($<1\%$) as the primary impurities. Conformal deposition when using NH_3 plasma is a strong advantage of chlorosilane precursors. Unfortunately, the WER for SiN_x deposited with chlorosilane precursors is reported to be high, and film density is low due to hydrogen incorporation. Recently, a new chlorosilane precursor, pentachlorodisilane (PCDS) has been reported¹¹ that while similar to HCDS, results in a 20% higher GPC (0.78 vs. 1.02 \AA/cycle) with similar or better physical properties. Substituting a chlorine atom with a hydrogen appears to lower the steric hindrance of the PCDS molecule and increase its polarity, leading to a precursor with higher reactivity. In addition, a precursor exposure of only $4 \times 10^4\text{ L}$,

or 4–5 orders of magnitude lower than the exposure for thermal ALD processes and 1–2 orders lower than that of other PEALD provides results with a similar GPC. The unique hollow cathode plasma source used for films grown with both HCDS and PCDS results in exceptionally low oxygen contamination in these films.

Organosilanes

The first organosilane used for SiN_x ALD was tris(dimethylamino) silane (TDMAS, **Cat. Nos. 570133, 759562**) in 2008.¹² Using a remote ICP nitrogen-forming gas plasma to successfully deposit SiN_x , though with carbon impurities of 5–10%. Provine et al.¹³ improved on these results and were able to grow SiN_x with high film density (2.4 g/cm^3) and low WER (3 nm/min in 100:1 HF) at a temperature of 350 °C. Performing a hydrogen plasma post-anneal reduced WER to less than 1 nm/min.

Bis(tert-butylamino)silane (BTBAS) is another aminosilane frequently used for SiN_x deposition. Knoops et al. deposited high quality SiN_x with BTBAS and N_2 plasma.¹⁴ Film density was very high at 2.8 g/cm^3 , and film wet etch rate was 0.2 nm/min for growth at 400 °C. Carbon contamination was less than 2%, but that increased to approximately 10% for films grown at 200 °C. Film properties were similar to those obtained from low-pressure chemical vapor deposition (LPCVD) grown SiN_x , which is attributed to the high film density of the film.

All organosilane precursors using nitrogen plasma, causes the GPC to drop to nearly zero. When NH_3 plasma is used, $-\text{NH}_2$ is a common surface termination. Huang et al.¹⁵ predicted a high activation energy barrier for BTBAS and other amine groups, and this prediction was experimentally confirmed by Provine for TDMAS and NH_3 plasma growth. Density functional theory simulations predicted that BTBAS would only adsorb at undercoordinated nitrogen or silicon sites, which NH_3 plasma cannot provide. Another issue with most organosilanes is the low GPC — typically less than 0.3 Å/cycle. Organosilanes are large molecules that provide only a single silicon atom, so steric hindrance likely plays a role, though the requirement for undercoordinated surface sites probably hinders growth as well. Finally, conformality over HAR structures is limited for organosilanes. Faraz et al. found at best 50% conformality for sidewalls (26 vs 13 nm) when using di(sec-butylamino)silane (DSBAS) and N_2 plasma.¹ These results are common, and are likely due to the soft saturation observed for N_2 plasma exposure. Typically sidewalls are exposed to lower plasma density during the deposition process compared to the top and bottom of the structure.

Heterosilanes

The last group of precursors encompasses all non-organic and non-halide precursors. Silica is simplest of the precursors and has already been discussed. Well-known for use its use in PECVD, SiN_x can be deposited using SiH_4 and N_2 plasma.¹⁶ The disadvantage of this approach is the long (60 s) N_2 plasma time required for saturation. Likewise, S-H contamination is problematic and likely results in low film density and high WER. Trisilylamine (TSA) is another Si precursor that has been

investigated for SiN_x deposition. Triyoso et al.¹⁷ demonstrated the growth of SiN_x with TSA and N_2/H_2 plasma at 300 and 400 °C. GPC depended greatly on plasma conditions, and varied from 1.3 to 2.1 Å/cycle and WER in 100:1 HF was approximately 1 nm/min. When comparing PEALD SiN_x with PECVD SiN_x , they found TSA-based PEALD improved transistor performance with higher drive current, higher hole mobility, and improved $I_{\text{on}}/I_{\text{off}}$ ratio. Jang et al.¹⁸ deposited SiN_x with TSA and NH_3 plasma, though with a lower GPC (0.6 Å/cycle vs. ~ 1.5 Å/cycle). This has important implications for conformal deposition over HAR structures, since NH_3 plasma offers improved step coverage. Finally, neopentasilane (NPS) and N_2 plasma were used to grow SiN_x between 250 and 300 °C.¹⁹ Film properties were found to be similar to that of TSA, though NPS has a slightly higher GPC (1.2 vs. 1.4 Å/cycle). The WER for SiN_x grown with NPS was strongly plasma dependent, but optimized conditions resulted in a WER of between 2 and 3 nm/min. Both TSA and NPS are interesting precursors due to their high silicon percentage relative to molecular weight, and they offer higher GPC than organosilanes while maintaining a lower WER than typical chlorosilanes.

Summary and Outlook

The need for high quality, conformal SiN_x films grown at low temperature is increasing, and both academia and industry are working to develop advanced processes and precursors. Currently available precursors offer a range of advantages and disadvantages. Chlorosilanes provide enhanced GPC and conformality over HAR structures, but lack wet etch resistance and film density. Organosilanes enable the growth of SiN_x films with extremely low WER, comparable to or lower than those achieved with LPCVD, but are hindered by low GPC and poor conformality. The heterosilanes, which include trisilylamine and neopentasilane, offer both good GPC, which aids in throughput, and low WER. Further investigation is needed to see if these precursors can deliver conformality over HAR structures.

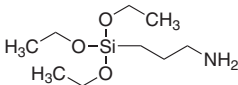
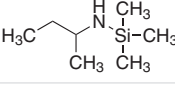
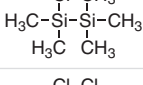
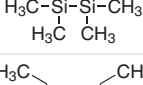
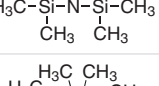
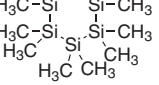
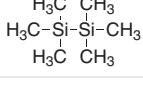
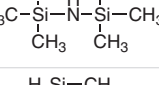

While not a silicon precursor, it is worth discussing current work on nitrogen sources. Recent advances in hydrazine delivery technology have enabled the use of ultra-high purity hydrazine in thermal ALD. While toxicity is still a concern, the overall safety of the source has been improved.²⁰ Thermal ALD of TaN and WN with hydrazine as the nitrogen source has been demonstrated. Likewise, low resistivity of TiN deposited at 275–350 °C has been reported. Few reports exist regarding the deposition of SiN_x with hydrazine, but the growth of SiN_x passivation layers using HCDS and hydrazine at 285 °C has been successful.²¹ Chlorine contamination is a problem; these issues can likely be associated with the extremely low deposition temperature since similar issues occur for PEALD below 300 °C. Current work using ultra-high purity hydrazine as a source for SiN_x deposition is promising, and good SiN_x properties have been obtained in depositions occurring between 350 and 400 °C, which should enable the development of low temperature thermal ALD of SiN_x . Together, improvements in nitrogen sources and silicon precursors portend a bright future for atomic layer deposition of SiN_x .

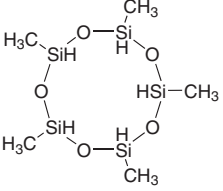
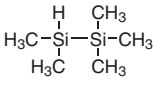
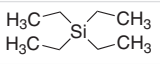
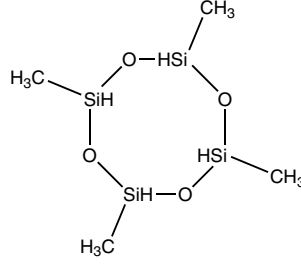
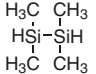
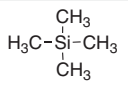
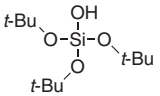
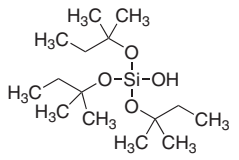
References

- (1) Faraz, T.; van Drunen, M.; Knoops, H. C.; Mallikarjunan, A.; Buchanan, I.; Hausmann, D. M.; Henri, J.; Kessels, W. M. *ACS Appl. Mater. Interfaces* **2017**, *9* (2), 1858–1869.
- (2) Meng, X.; Byun, Y. C.; Kim, H. S.; Lee, J. S.; Lucero, A. T.; Cheng, L.; Kim, J. *Materials (Basel)* **2016**, *9* (12).
- (3) Morishita, S.; Sugahara, S.; Matsumura, M. *Appl. Surf. Sci.* **1997**, *112*, 198–204.
- (4) Park, K.; Yun, W.-D.; Choi, B.-J.; Kim, H.-D.; Lee, W.-J.; Rha, S.-K.; Park, C. O. *Thin Solid Films* **2009**, *517* (14), 3975–3978.
- (5) Nakajima, A.; Yoshimoto, T.; Kidera, T.; Obata, K.; Yokoyama, S.; Sunami, H.; Hirose, M. *Appl. Phys. Lett.* **2000**, *77* (18), 2855–2857.
- (6) Hansch, W.; Nakajima, A.; Yokoyama, S. *Appl. Phys. Lett.* **1999**, *75* (11), 1535–1537.
- (7) Riedel, S.; Sundqvist, J.; Gumprecht, T. *Thin Solid Films* **2015**, *577*, 114–118.
- (8) Profijt, H. B.; Potts, S. E.; van de Sanden, M. C. M.; Kessels, W. M. M. *J. Vac. Sci. Technol. A* **2011**, *29* (5), 050801.
- (9) Nagata, K.; Nagasaka, M.; Yamaguchi, T.; Ogura, A.; Oji, H.; Son, J.-Y.; Hirose, I.; Watanabe, Y.; Hirota, Y. *ECS Transactions* **2013**, *53* (3), 51–56.
- (10) Ovanesyan, R. A.; Hausmann, D. M.; Agarwal, S. *ACS Appl. Mater. Interfaces* **2015**, *7* (20), 10806–10813.
- (11) Meng, X.; Kim, H. S.; Lucero, A. T.; Hwang, S. M.; Lee, J. S.; Byun, Y.-C.; Kim, J.; Hwang, B. K.; Zhou, X.; Young, J.; Telgenhoff, M. *ACS Appl. Mater. Interfaces* **2018**, *10* (16), 14116–14123.
- (12) F. Q. and H. C., in *Silicon Nitride and Silicon Oxide Thin Films by Plasma ALD*, Bruges, Belgium, **2008** (Proceedings of the 8th International Conference on Atomic Layer Deposition).
- (13) Provine, J.; Schindler, P.; Kim, Y.; Walch, S. P.; Kim, H. J.; Kim, K.-H.; Prinz, F. B. *AIP Adv.* **2016**, *6* (6), 065012.
- (14) Knoops, H. C.; Braeken, E. M.; de Peuter, K.; Potts, S. E.; Haukka, S.; Pore, V.; Kessels, W. M. *ACS Appl. Mater. Interfaces* **2015**, *7* (35), 19857–62.
- (15) Huang, L.; Han, B.; Han, B.; Dereskei-Kovacs, A.; Xiao, M.; Lei, X.; O'Neill, M. L.; Pearlstein, R. M.; Chandra, H.; Cheng, H. *Phys. Chem. Chem. Phys.* **2014**, *16* (34), 18501–18512.
- (16) King, S. W. *J. Vac. Sci. Technol. A* **2011**, *29* (4), 041501.
- (17) Triyoso, D. H.; Hempel, K.; Ohsiek, S.; Jaschke, V.; Shu, J.; Mutas, S.; Dittmar, K.; Schaeffer, J.; Utess, D.; Lenski, M. *ECS J. Solid State Sci. Technol.* **2013**, *2* (11), N222–N227.
- (18) Jang, W.; Jeon, H.; Song, H.; Kim, H.; Park, J.; Kim, H.; Jeon, H. *Phys. Status Solidi A* **2015**, *212* (12), 2785–2790.
- (19) Weeks, S.; Nowling, G.; Fuchigami, N.; Bowes, M.; Littau, K. *J. Vac. Sci. Technol. A* **2016**, *34* (1), 01A140.
- (20) Alvarez, D.; Spiegelman, J.; Holmes, R.; Andachi, K.; Raynor, M.; Shimizu, H. *ECS Transactions* **2017**, *77* (5), 219–225.
- (21) Edmonds, M.; Sardashti, K.; Wolf, S.; Chagarov, E.; Clemons, M.; Kent, T.; Park, J. H.; Tang, K.; McIntyre, P. C.; Yoshida, N.; Dong, L.; Holmes, R.; Alvarez, D.; Kummel, A. C. *J. Chem. Phys.* **2017**, *146* (5), 052820.

Silicon ALD Precursors

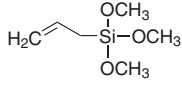
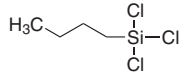
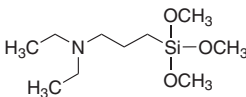
For a complete list of available materials, visit SigmaAldrich.com/vapordeposition.

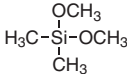
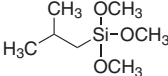
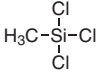
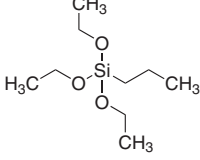
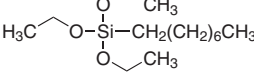
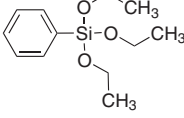
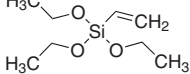
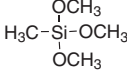
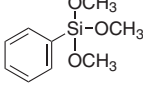
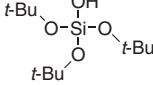
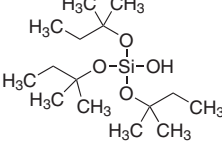
Name	Structure	Purity (%) Or Grade	Form	Cat. No.
(3-Aminopropyl)triethoxysilane		≥98.0%	liquid	741442-100ML 741442-500ML
<i>N</i> -sec-Butyl(trimethylsilyl)amine		98%	liquid	654671-5G
Chloropentamethyldisilane		97%	liquid	490407-5G
1,2-Dichlorotetramethyldisilane		95%	liquid	415456-5ML
1,3-Diethyl-1,1,3,3-tetramethyldisilazane		>98.0%	liquid	646261-1G 646261-5G
Dodecamethylcyclohexasilane		≥97%, GC	powder or crystals	437492-1G
Hexamethyldisilane		98%	liquid	217069-5G 217069-10G 217069-50G
Hexamethyldisilazane		99.9%	liquid	379212-25ML 379212-100ML
		≥99%	liquid	440191-100ML 440191-1L
Methylsilane		≥99.9%	liquid	462993-10G 462993-20G

Name	Structure	Purity (%) Or Grade	Form	Cat. No.
2,4,6,8,10-Pentamethylcyclopentasiloxane		96%	liquid	517801-25ML
Pentamethyldisilane		97%	liquid	557641-5ML
Silicon tetrabromide	SiBr ₄	99.995% trace metals basis	liquid	494100-5ML 494100-25ML
		99%	liquid	333468-10G
Silicon tetrachloride	SiCl ₄	99.998% trace metals basis	liquid	289388-100ML 289388-800ML
		99.998% trace metals basis, packaged for use in deposition systems	liquid	688509-25ML
		99%	liquid	215120-100G 215120-1KG
Tetraethylsilane		99%	liquid	510874-5ML
2,4,6,8-Tetramethylcyclotetrasiloxane		≥99.999% trace metals basis ≥98.5%	liquid	512990-25ML 512990-100ML
1,1,2,2-Tetramethyldisilane		98%	liquid	445126-1G
Tetramethylsilane		≥99.99% trace metals basis	liquid	523771-100ML
Tris(<i>tert</i> -butoxy)silanol		packaged for use in deposition systems	solid	697281-25G
Tris(<i>tert</i> -pentoxy)silanol		packaged for use in deposition systems	liquid	697303-25G

Silicon Solution Deposition Precursors

For a complete list of available materials, visit [SigmaAldrich.com/solutiondeposition](https://www.sigmaaldrich.com/solutiondeposition).

Name	Structure	Purity (%) Or Grade	Cat. No.
Allyltrimethoxysilane		≥98%	679267-50G
Butyltrichlorosilane		≥98%	679224-50G
[3-(Diethylamino)propyl]trimethoxysilane		≥98%	679356-50G

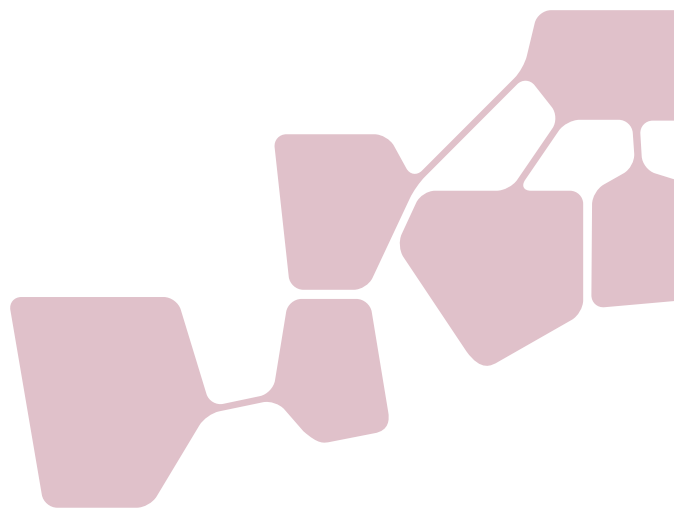
Name	Structure	Purity (%) Or Grade	Cat. No.
Dimethoxydimethylsilane		≥99.5% 99.999% metals basis	556688-25ML
Isobutyl(trimethoxy)silane		≥98%	679364-50G
Methyltrichlorosilane		≥98%, GC ≥99.99% (as metals)	679208-50G
<i>n</i> -Propyltriethoxysilane		≥98%	679321-50G
Triethoxy(octyl)silane		99.99% trace metals basis 98%	679305-50G
Triethoxyphenylsilane		≥98%	679291-50G
Triethoxyvinylsilane		≥98%	679275-50G
Trimethoxymethylsilane		≥98%	679232-50G
Trimethoxyphenylsilane		98%	679313-50G
Tris(<i>tert</i> -butoxy)silanol		99.999%	553468-5G 553468-25G
Tris(<i>tert</i> -pentoxy)silanol		≥99.99%	553441-5G 553441-25G

Group 11 Thin Films by Atomic Layer Deposition



Sean Barry

Department of Chemistry, Carleton University, Ottawa,
Ontario K1S 5B6, Canada
Email: sean_barry@carleton.ca



Introduction

Copper metal deposition processes are an essential tool for depositing interconnects used in microelectronic applications, giving group 11 (coinage metals: Copper, Silver, and Gold) an important place in atomic layer deposition (ALD) process development. A significant amount of development has been invested in the design and improvement of both processes and precursors of Cu^+ and Cu^{2+} oxidation states over the last 20 years (see Figure 1).

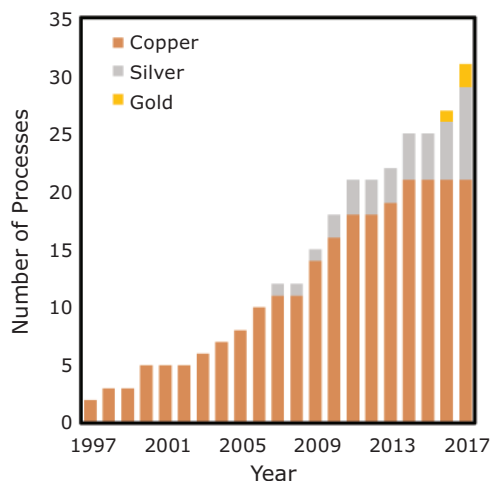


Figure 1. The cumulative number of coinage metal ALD processes developed over the past 20 years.

The timeline for the development of silver and gold metal deposition precursors roughly follows their standard potentials (Table 1). This is probably due to ease of synthesis and isolation, since the reactivity of metal deposition precursors is loosely governed by their standard potential. A key element of precursor development is testing thermal stability, so processes involving Ag^+ and Au^{3+} were quickly developed, but many high potential cations have still not been successfully incorporated into precursors.

Table 1. The standard potentials (against a hydrogen electrode) for the common cations of the coinage metals.

Redox Half Reaction	Standard Potential, E^0 (V)
$\text{Ag}^{2+} + 2 e^- \rightarrow \text{Ag}^0$	1.98
$\text{Au}^+ + e^- \rightarrow \text{Au}^0$	1.69
$\text{Au}^{3+} + 3 e^- \rightarrow \text{Au}^0$	1.40
$\text{Ag}^+ + e^- \rightarrow \text{Ag}^0$	0.80
$\text{Cu}^+ + e^- \rightarrow \text{Cu}^0$	0.52
$\text{Cu}^{2+} + 2 e^- \rightarrow \text{Cu}^0$	0.34

In this article, we will discuss coinage metal deposition processes in order to provide a sense of the most critical precursors, reducing agents, and processes. This review is not comprehensive, but rather a brief perspective on the current state of the art. For a more in-depth discussion on precursor and process tabulation see the recent review by Puurunen.

Copper

Copper metal has been very well studied and a tremendous number of copper-based precursors have been developed, including halides, amidinates, guanidinates, β -diketonates, and aminoalkoxides (Figure 2).¹ In general, thermal copper depositions can occur over a wide temperature range (120–500 °C), while plasma and catalyzed depositions occur as low as room temperature, with the energy necessary for the process being supplied by the plasma, or circumvented by the catalyst. Interestingly, many depositions of copper by ALD start to exhibit non-self-limited, continuous growth (i.e., chemical vapor deposition, CVD) at 200–230 °C. Precursor examples (Figure 2) include Cu^+ centers but are dominated by Cu^{2+} .

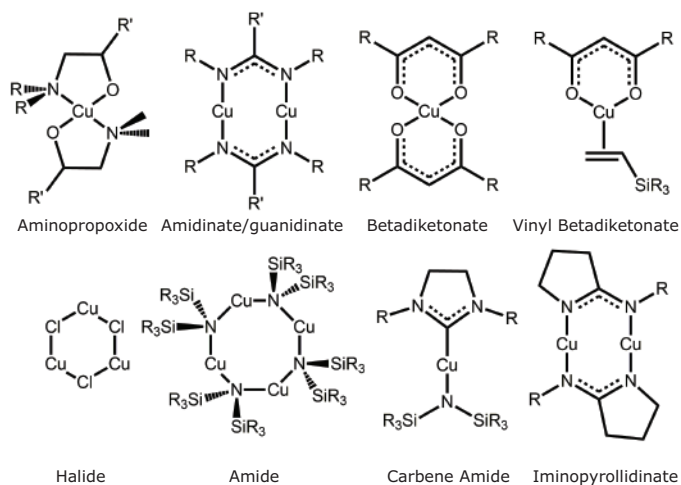


Figure 2. A representative array of currently available precursors for copper metal deposition.

The Cu^{2+} dication is reduced relatively easily to copper metal measured against the oxidation of H_2 , but Cu^{2+} is the most difficult to reduce of any of the common oxidation states of any coinage metal. This might account for the tendency of copper precursors to have chemisorbed moieties containing Cu^+ , even if the precursor contained Cu^{2+} (see **Table 1**). A good example of this phenomenon can be seen with the copper(II) aminoalkoxides (**Figure 3**).

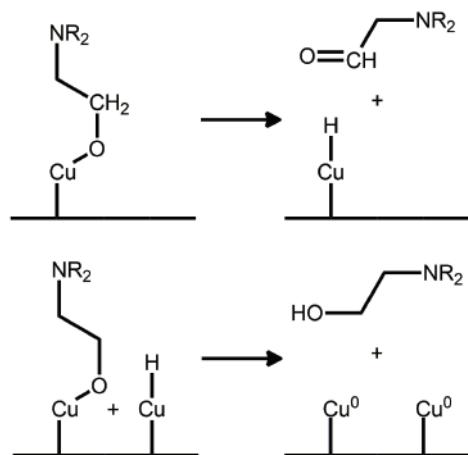


Figure 3. Thermal dehydrogenation of an aminoalkoxide at a surface copper.

The mechanism for the thermal dehydrogenation of an aminoalkoxide at a copper surface was first elucidated in 1993 and the model for chemisorption was published in 2012. The model described chemisorption of the Cu^+ species, while experimental work completed in 1996 demonstrated the presence of both the aldehyde and the alcohol from the aminopropoxide ligand. This thermal behavior is not self-limiting, yet Bis(dimethylamino-2-propoxy)copper(II) ($\text{Cu}(\text{DMAP})_2$) has been shown to undergo ALD using a variety of reducing agents including diethyl zinc, formic acid/hydrazine, and

boranedimethylamine. The additional methyl group in the beta position prevents aldehyde formation and arrests thermal decomposition. The DMAP precursor is still able to undergo ALD growth, including by reaction with amino borane, which is essentially a source of hydrogen at the reaction temperature to produce copper metal at the surface (**Figure 4**).⁷

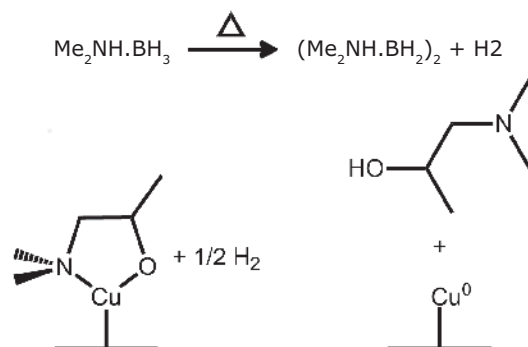


Figure 4. A copper DMAP surface moiety can be reduced to metallic copper and the parent ligand by dihydrogen generated from the thermal decomposition of borane dimethylamine.

An interesting note about $\text{Cu}(\text{DMAP})_2$ is that it has covalently bonded oxygen. From a precursor design point of view, this bonding arrangement is generally avoided since any atom bonded directly to the metal center is at considerable risk of becoming incorporated in the metal film as an impurity. Obviously, in the case of this precursor, this is unfounded.

Silver

Silver metal ALD processes are much scarcer due to silver's lower standard potential and thus lower reactivity. It can be difficult to design a silver-containing precursor that has the thermal (and photo) stability to withstand volatilization. The first silver metal deposited by ALD was in 2007, from a phosphine-supported silver(I) carboxylate. This process had a growth rate of 1.2 Å/cycle, but was only viable at 140 °C due to both volatility and a low thermal decomposition temperature of the precursor. Additionally, significant impurities were observed in the resulting film, including 10% oxygen contamination.

In 2014, trimethylphosphine-supported silver(I) hexafluoroacetoacetate was shown to undergo thermal ALD of silver metal using both formalin (aqueous formaldehyde stabilized with methanol) in an two step type process, and with trimethylaluminum (TMA, **Cat. No. 663301**) and water in three step process. In the first instance, the silver metal had a growth rate of 0.7 Å/cycle at 200 °C, although it showed somewhat slower growth at 170 °C. With TMA and water, the growth rate was significantly lower, about 0.2 Å/cycle at 110 °C. Interestingly, the growth rate could be improved with multiple, sequential doses of TMA/water, which appeared not to show saturation. The authors speculated that the TMA and water pulses were removing hexafluoroacetoacetate moieties from the surface, allowing better nucleation of the incoming precursor.

The precursor hexafluoroacetylacetonato 1,5-cyclooctadiene silver(I) (hfacAg^ICOD, **Cat. No. 348198**) is another early example of silver metal deposited by thermal ALD used by injection of the precursor dissolved in toluene, followed by a propanol wash. The publication does not describe the ALD process in detail, but suggests the propanol undergoes oxidative dehydrogenation (possibly catalysed by the silver metal) and that this is responsible for the reduction of the silver (**Figure 5**).

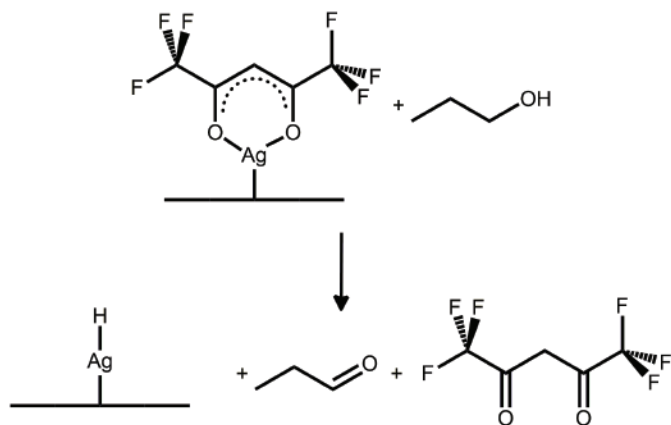
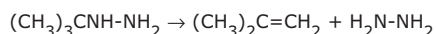


Figure 5. The oxidative dehydrogenation of propanol to produce a silver hydride moiety at a substrate surface.

The process was further investigated to determine the ALD process parameters and surface chemistry, highlighting several mechanistic points. First, it showed the cyclooctadiene is lost either in solution or during volatilization, emphasizing the surface moiety should be Ag^Ihfac (**Figure 5**). Second, the ALD temperature window was very small (between 121–130 °C) and any deviation adds a CVD element to the growth. Finally, the silver hydride surface was shown to improve the kinetics of monolayer formation when carried through to the introduction of the hfacAg^ICOD. This result was also predicted computationally to enhance coverage. Ultimately, the process results in a nominal growth rate of 0.16 Å/cycle when run at 125 °C, which is low considering that chemisorption might be partially aided by the existence of a surface hydride. This same precursor shows similar growth rates (0.20 Å/cycle) over a slightly larger temperature window (105–128 °C) when tertbutylhydrazine was used instead of propanol. The enhanced process characteristics are thought to be due to the thermal rearrangement of tertbutylhydrazine to hydrazine and isobutene, where hydrazine undergoes oxidative dehydrogenation much more readily than propanol:



A similar silver compound (Ag^I(fod)PEt₃) was shown to deposit silver metal using hydrogen plasma as the reducing agent. The process was viable over a small temperature range: at 120 °C, saturative growth was shown to be 0.3 Å/cycle, and at 140 °C, it was 0.4 Å/cycle. The same precursor was used with methylamine–borane (BH₃(NMe₂H)) as the reducing agent and

showed saturative growth between 104 °C and 130 °C with a rate of 0.3 Å/cycle. One benefit of using Ag^I(fod)PEt₃ is the ease of its synthesis. Starting with AgO, the precursor can be made in 96% yield using standard Schlenk techniques.

Deposition of Ag^I(fod)PEt₃ can also be achieved using a plasma generated from ammonia gas. Interestingly, when plasma ammonia is used, the authors report the growth rate increased significantly to 2.4 Å/cycle and the oxygen impurity decreased to 2%. Nitrogen impurity was shown to increase from 2% to 7% when using hydrogen plasma with the use of plasma ammonia. The authors attributed both the improved growth rate and nitrogen impurity to a longer lived amine defect on the silver surface that allows better nucleation of the silver precursor on the surface. In contrast, the hydrogen-terminated silver likely has a shorter lifetime, and so nucleation of Ag^I(fod)PEt₃ is not as kinetically viable, resulting in a low growth rate (**Figure 6**).

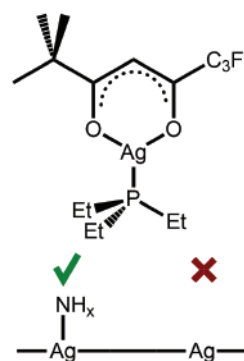


Figure 6. The nucleation of Ag^I(fod)PEt₃ was found to occur more readily with an amine-terminated surface than with a clean silver metal surface.

Gold

Gold metal processes by ALD are very rare — only two have been published to date. The first used Me₃Au^{III}PMMe₃ (**Figure 7**) and oxygen plasma, followed by water. This three step process has a growth rate of 0.5 Å/cycle and a narrow ALD window of 120–130 °C, with CVD occurring at higher temperatures. Interestingly, this process produces a film containing gold and phosphorous in the absence of the water pulse, and requires the water to convert the P₂O₅ formed by oxygen plasma exposure to H₃PO₄, which becomes a volatile by-product. The second gold ALD process uses Me₂Au^{III}(S₂CNEt₂) (**Figure 7**) and ozone to produce gold metal with a growth rate of 1.1 Å/cycle. In this process, the ALD window is broader and reaches a higher temperature (120–200 °C), and the growth rate is significantly higher than the first process. Another significant difference in these processes is in the precursors: Me₃Au^{III}PMMe₃ is a liquid at room temperature that can be synthesized with an overall 93% purified yield, while Me₂Au^{III}(S₂CNEt₂) is a room temperature solid with an overall purified yield of ~10%. However, gold metal is now accessible from both plasma and thermal ALD processes, with reasonable growth rates. Although there is still much room for improvement, thus indicates that gold can now be considered an ALD-accessible metal.

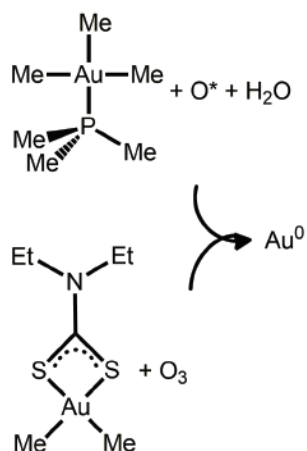


Figure 7. The two currently available processes for the deposition of gold metal by ALD.

Conclusions

The three coinage metals (copper, silver and gold) are all accessible through multiple ALD processes. Copper processes are the most well-developed, due to the commercial use of copper metal interconnects on the nanometer scale, coupled with the straightforward synthetic chemistry of copper-containing inorganic and organometallic compounds. There are a large number of copper precursors with various ligands, and processes include thermal methods at a variety of temperatures as well as plasma processes that can be used to deposit copper metal reliably. Presently, the preferred copper precursor appears to be $\text{Cu}^{\text{II}}(\text{DMAP})$, due to its ease of synthesis, versatility of deposition processes, and the low impurity of the resulting films.

Silver and gold metal deposition processes are less mature than processes using copper. Silver metal has been deposited by a variety of β -diketonate precursors, with fluorinated ligands showing the best results. Several of the silver processes have been very well characterized, and this should allow additional improvement of silver-containing ALD precursors.

For gold, the only two currently available processes cover thermal and plasma, but development has really just begun. The first true gold metal process was introduced in 2016, with the second following in 2017. Further understanding of both processes is required, and further precursor development will certainly help address the specific challenges for deploying gold across a wider temperature window with increased possibilities for surface chemistry. The lessons learned about copper ALD can now be applied to deposition of silver and gold, and the possibilities are just beginning to be explored.

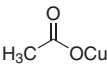
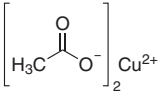
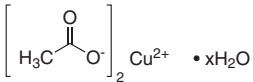
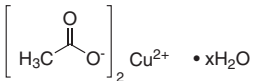
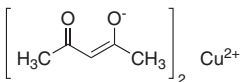
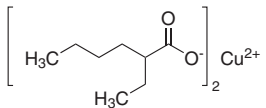
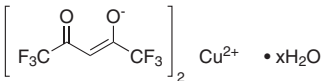
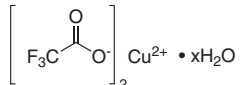
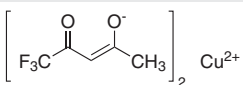
References

- (1) Gordon, P. G.; Kurek, A.; Barry, S. T. *ECS JSS* **2015**, 4, N3188–N3197.
- (2) Miikkulainen, V.; Leskelä, M.; Ritala, M.; Puurunen, R. L. *J. Appl. Phys.* **2013**, 113, 021301.
- (3) Young, V. L.; Cox, D. F.; Davis, M. E. *Chem. Mater.* **1993**, 5, 1701–1709.
- (4) Elliott, S. D.; Dey, G.; Maimaiti, Y. J. *Chem. Phys.* **2017**, 146, 052822.
- (5) Lee, B. H.; Hwang, J. K.; Nam, J. W.; Lee, S. U.; Kim, J. T.; Koo, S. M.; Baunemann, A.; Fischer, R. A.; Sung, M. M. *Angew. Chem. Int. Ed. Engl.* **2009**, 48, 4536–4539.
- (6) Knisley, T. J.; Ariyasena, T. C.; Sajavaara, T.; Saly, M. J. Winter, C. H. *Chem. Mater.* **2011**, 23, 4417–4419.
- (7) Kalutarage, L. C.; Clendenning, S. B.; Winter, C. H. *Chem. Mater.* **2014**, 26, 3731–3738.
- (8) Niskanen, A.; Hatanpää, T.; Arstila, K.; Leskelä, M.; Ritala, M. *Chem. Vap. Deposition* **2007**, 13, 408–413.
- (9) Masango, S. S.; Peng, L.; Marks, L. D.; Van Duyne, R. P.; Stair, P. C. J. *Phys. Chem. C* **2014**, 118, 17655–17661.
- (10) Chalker, P. R.; Romani, S.; Marshall, P. A.; Rosseinsky, M. J.; Rushworth, S.; Williams, P. A. *Nanotechnology* **2010**, 21, 1–7.
- (11) Golrokhi, Z.; Chalker, S.; Sutcliffe, C. J.; Potter, R. J. *Appl. Surf. Sci.* **2016**, 364, 789–797.
- (12) Golrokhi, Z.; Marshall, P. A.; Romani, S.; Rushworth, S.; Chalker, P. R.; Potter, R. J. *Appl. Surf. Sci.* **2017**, 399, 123–131.
- (13) Kariniemi, M.; Niinistö, J.; Hatanpää, T.; Kemell, M.; Sajavaara, T.; Ritala, M.; Leskelä, M. *Chem. Mater.* **2011**, 23, 2901–2907.
- (14) Mäkelä, M.; Hatanpää, T.; Mizohata, K.; Meinander, K.; Niinistö, J.; Räisänen, J.; Ritala, M.; Leskelä, M. *Chem. Mater.* **2017**, 29, 2040–2045.
- (15) Minjauw, M. M.; Solano, E.; Sree, S. P.; Asapu, R.; Van Daele, M.; Ramachandran, R. K.; Heremans, G.; Verbruggen, S. W.; Lenaerts, S.; Martens, J. A.; Detavernier, C.; Dendooven, J. *Chem. Mater.* **2017**, 29, 7114–7121.
- (16) Griffiths, M. B. E.; Pallister, P. J.; Mandia, D. J.; Barry, S. T. *Chem. Mater.* **2016**, 28, 44–46.
- (17) Mäkelä, M.; Hatanpää, T.; Mizohata, K.; Räisänen, J.; Ritala, M.; Leskelä, M. *Chem. Mater.* **2017**, 29, 6130–6136.

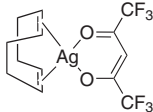
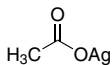
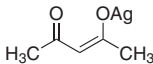
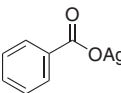
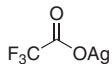
Group 11 Precursors

For a complete list of available materials, visit [SigmaAldrich.com/solutiondeposition](https://www.sigmaaldrich.com/solutiondeposition).

Copper

Name	Structure	Purity (%) Or Grade	Form	Cat. No.
Copper(I) acetate		97%	powder and chunks	403342-1G 403342-10G
Copper(II) acetate		99.99% trace metals basis	powder	517453-5G 517453-25G
		98%	powder or crystals	326755-25G 326755-100G
Copper(II) acetate monohydrate		99.99% trace metals basis	powder or crystals	229601-10G 229601-50G
Copper(II) acetate hydrate		98%	crystals	341746-100G 341746-500G 341746-2.5KG
Copper(II) acetylacetonate		≥99.9% trace metals basis	powder	514365-10G 514365-50G
		97%	powder	C87851-25G C87851-100G C87851-500G
Copper(II) 2-ethylhexanoate		-	powder or chunks	337323-5G 337323-25G
Copper(II) hexafluoroacetylacetonate hydrate		-	powder or chunks	335193-5G
Copper(II) trifluoroacetate hydrate		-	powder or chunks	311189-5G
Copper(II) trifluoroacetylacetonate		97%	solid	101826-5G

Silver

Name	Structure	Purity (%) Or Grade	Form	Cat. No.
(1,5-Cyclooctadiene) (hexafluoroacetylacetonato)silver(I)		99%	powder	348198-5G
Silver acetate		99.99% trace metals basis	powder or crystals	204374-10G 204374-50G
Silver acetylacetonate		98%	solid	323489-1G 323489-5G
Silver benzoate		99%	powder or crystals	227277-10G 227277-50G
Silver trifluoroacetate		≥99.99% trace metals basis	liquid	482307-1G 482307-2.5G 482307-10G
		98%	powder	T62405-5G T62405-25G

Gold

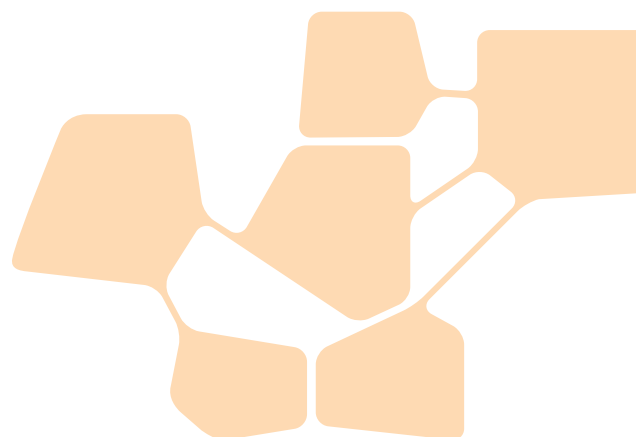
Name	Structure	Purity (%) Or Grade	Form	Cat. No.
Gold(I) cyanide	AuCN	99.9% trace metals basis	powder	254088-1G

Few Monolayer Atomic Layer Deposition (ALD) on Surfaces and Interfaces for Energy Applications



Peifu Cheng, Parag Banerjee*

Department of Mechanical Engineering and Materials Science
One Brookings Drive, Washington University in St. Louis, St. Louis, MO 63130
*Email: parag.banerjee@wustl.edu



Introduction

Atomic layer deposition (ALD) exploits a sequential set of two or more surface reactions repeated cyclically to achieve thin film growth.¹ These surface reactions occur between a chemisorbed species attached to a substrate and incoming precursor molecules from the gas-phase. Due to its precise deposition mechanism, ALD possesses many advantages over other thin film deposition processes. First, ALD offers extremely precise control at the angstrom level over the thickness of the deposited layer. Second, ultrahigh-aspect-ratio structures, including nanoporous solids² and three-dimensional (3D) hierarchical structures,³ can be conformally and uniformly covered by ALD without thickness or composition gradients. Third, the chemical composition of films can be controlled by tailoring ALD cycles in a programmable manner.^{4,5} Finally, ALD enables deposition at lower temperatures,⁶ making it possible to use with polymer-based⁷ and biological substrates that are incompatible with higher temperatures.⁸

It is not widely appreciated that only a few monolayers of material added to a surface or interface can significantly impact performance, quality, and reliability. Since ALD allows atomic scale resolution in deposition of monolayers, new scientific mechanisms and phenomena can be investigated by characterizing these surfaces. While there are many excellent review articles on applied ALD research,⁹⁻¹⁷ none focus on the impact of few monolayer ALD films on materials and devices. Therefore, this review highlights research using few monolayer ALD to enhance material and device quality, performance, and reliability, specifically in the fields of photovoltaics, batteries, and catalysis.

We define “few monolayers” as less than 10 layers or a thickness of less than 2–3 nm. This demarcation of a ‘few’ is based on research reviews, which show impressive improvements in performance and reliability within this thickness range, and in most instances actual performance suppression by a thicker film. This definition also includes descriptions such as ultrathin, thin, compact, and few layer.

Photovoltaics

ALD has been used to suppress charge recombination at interfaces in photovoltaic devices such as hybrid organic-inorganic perovskite solar cells, dye-sensitized solar cells (DSSCs), and quantum dot solar cells (QDSCs). Also, with the advent of hybrid organic-inorganic perovskite solar cells, ALD has been effectively used to improve the stability of these air sensitive compounds.

TiO₂ (up to four nm) was deposited by ALD on spin-coated mesoporous nanoparticulate TiO₂ films as blocking layers to make high efficiency solid-state perovskite-based (CH₃NH₃PbI₃) solar cells.¹⁸ As shown in **Figure 1A**, a two nm conformal TiO₂ ALD overlayer was sufficient to block the electron recombination, leading to a large open-circuit potential of 969.4 mV (reference potential 836.6 mV) and the high photon-to-current efficiency (PCE) of 11.5%.

Few layer ALD has been employed to enhance the PCE of DSSCs.¹⁹⁻²² An ultrathin TiO₂ layer (10 cycles, 0.3–0.6 nm) was successfully coated on the surface of submicrometer-sized aggregates of ZnO nanocrystallites.¹⁹ As shown in **Figure 1B**, both the open-circuit voltage and the fill factor were increased

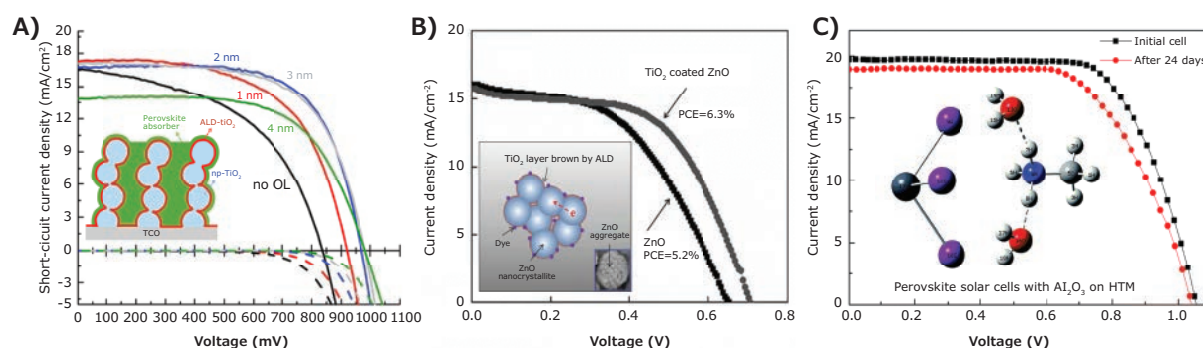


Figure 1. A) Two nm ALD TiO₂ on mesoporous TiO₂ is sufficient to block electron hole recombination in solid-state perovskite-based solar cells. Reproduced with permission from reference 18, copyright 2014 Wiley. B) 0.6 nm of ALD TiO₂ on nanocrystalline ZnO suppresses charge recombination in DSSCs. Reproduced with permission from reference 19, copyright 2010 Wiley. C) 0.3 nm Al₂O₃ improves ambient stability of hybrid organic-inorganic perovskite solar cells to up to 24 days. Reproduced with permission from reference 24, copyright 2015 Royal Society of Chemistry.

by the introduction of a TiO₂ layer, due to suppression of surface charge recombination, without impairing the photocurrent density. This resulted in a more than 20% enhancement of PCE from 5.2% to 6.3%.

Conformal TiO₂ interfacial layers with a thickness of 1.5, 2.2, and 3.2 nm were coated on CdS quantum dots (QDs) and N719 dyes to enhance the performance of quantum dot and dye co-sensitized solar cells.²³ The introduction of TiO₂ interfacial layers significantly enhanced the short-circuit current density and PCE by improving the stability of the QDs and reducing the electron recombination with the electrolyte. The highest PCE reported was 2.36%, a 41% improvement from the reference device, at the optimal TiO₂ thickness of 2.2 nm.

Ultrathin compact Al₂O₃ layers were introduced by ALD (1-7 cycles) onto a layer of hole-transport material (HTM) to improve the stability of hybrid organic-inorganic perovskite solar cells in humid conditions.²⁴ The experimental results shown in **Figure 1C** indicate that a 3-cycle (~0.3 nm) ALD Al₂O₃ layer greatly improved the ambient stability of organic-inorganic perovskite solar cells and retained 90% of the initial PCE after 24 days of storage in air. When the number of ALD cycles increased, the current decreased sharply, probably caused by a significant reduction in the quantum tunneling of the holes.

Batteries

Batteries face limitations in energy storage density, charging rate, cycling stability, safety, and cost.¹⁷ Few layer ALD can effectively address many of these issues. For example, nanosized LiCoO₂ powders were prepared by a molten salt method, and then coated directly using ALD (2 and 6 cycle) to make ultrathin conformal Al₂O₃ films (**Figure 2A**).²⁵ The nano-LiCoO₂ electrodes coated with 2 ALD cycles of Al₂O₃ (0.22 nm) delivered the highest discharge capacity of 133 mAh/g at a current rate of 1400 mA/g (7.8 C), corresponding to a 250% improvement in reversible capacity when compared to bare LiCoO₂ nanoparticles. The improved performance resulted from the suppression of cobalt dissolution from the LiCoO₂ by the

ALD Al₂O₃ film. However, coating nano-LiCoO₂ electrodes with 6 ALD cycles of Al₂O₃ decreased the rate performance, indicating that thick films resulted in poor Li⁺ conductivity.

Nanostructured anodes coated by few layer ALD have also shown enhanced rate performance and cycling stability.²⁶ Porous Fe₂O₃ nanorods anchored on nitrogen-doped graphene sheets (NGr) (**Figure 2B**) are one example. ALD was used to deposit two cycles of Al₂O₃ film (<1 nm) on the Fe₂O₃ nanorods anchored on NGr (NGr-M-I-2ALD). This anode displayed a first-cycle Coulombic efficiency of 89%, much higher than uncoated NGr-I-M (65%). Further, the stable capacity of the anodes (249 mAh/g) at 20 A/g was maintained for 200 cycles.

Few layer ALD was also used for cathode modification to improve the performance of a lithium-sulfur (Li-S) battery.²⁷ Al₂O₃ was deposited by ALD on a graphene-sulfur (G-S) composite electrode. The specific capacity (646 mAh/g) of a G-S composite cathode with 10 ALD cycles of Al₂O₃ film (~1 nm) after 100 charge/discharge cycles at 0.5 oC was 103% higher than that of bare G-S (**Figure 2C**). The coulombic efficiency, rate capability, and electrochemical stability of the G-S composite electrode were also significantly increased by ALD-Al₂O₃ coating.

Other examples of the use of few monolayer ALD in lithium ion batteries include direct deposition of Al₂O₃ on natural graphite particles (**Figure 2D**).²⁸ These electrodes exhibit improved capacity retention when compared to bare electrodes because the insulating Al₂O₃ layer blocks electron conduction paths between natural graphite particles and the current collector. Ultrathin Al₂O₃ layers were coated directly on Li metal foils without air exposure to produce anodes for Li symmetric cells. The Li metal anodes treated with 20 ALD cycles of Al₂O₃ (~2 nm) were used for up to 1259 cycles before failure, double the lifetime of non-treated anodes (control sample = 711 cycles) (**Figure 2E**).²⁹ Few layer ALD also helped prevent dendrite formation and improve the homogeneity of current distribution along the Li electrode/solid electrolyte interphase (SEI) interface.

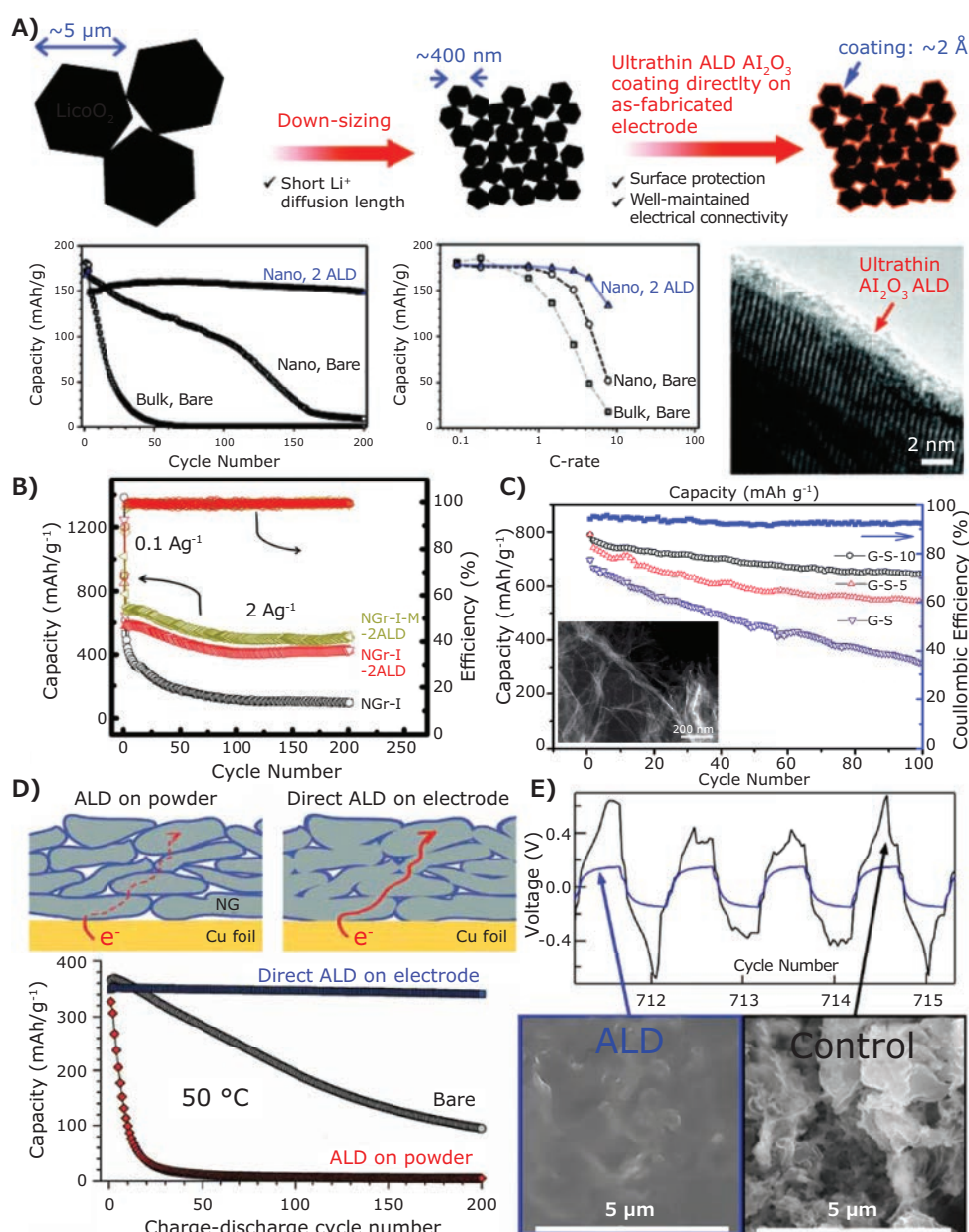


Figure 2. A) 0.2 nm Al_2O_3 coating on nanosized LiCoO_2 leads to increase capacity and stability. Reproduced with permission from reference 25, copyright 2011 American Chemical Society. B) High stability of 0.2 nm Al_2O_3 coated on Fe_2O_3 attached to N-doped graphene sheets (NGr-I-M-2ALD) maintained capacity for 200 cycles. Reproduced with permission from reference 26, copyright 2014 Elsevier. C) 1 nm Al_2O_3 deposited on graphene sulphur composite electrodes shows 103% high specific capacity compared to uncoated electrodes. Reproduced with permission from reference 27, copyright 2014 Royal Society of Chemistry. D) Direct deposition of Al_2O_3 on graphitic electrodes shows stable capacity behavior. Reproduced with permission from reference 28, copyright 2010 Wiley. Reproduced with permission from reference 29, copyright 2015 American Chemical Society. E) 2 nm Al_2O_3 on Li metal foils shows improved cyclability and prevents dendrite formation.

Catalysis

The challenges in catalyst development are improving catalytic activity, selectivity, and stability with minimal byproducts.¹⁴ Current synthetic methods, which include impregnation, ion exchange, and precipitation, are limited in facing these challenges because of the non-uniform distribution of surface sites and the relatively narrow set of starting materials available. Few monolayer ALD has been tested as a way to address these challenges.

Metal oxide catalysts with high catalytic activity and stability have been developed by few monolayer ALD.³⁰ TiO_2 thin films (15 nm) were deposited by ALD on supported Ag nanoparticles, while SiO_2 thin interlayers with thicknesses of 2, 5, 10, and 20 nm were deposited by ALD to separate the TiO_2 film from Ag nanoparticles. The photocatalytic activities of the samples and references were investigated by degradation of methylene blue (MB) in UV light illumination (Figure 3A). $\text{TiO}_2/\text{SiO}_2/\text{Ag}$ architectures with a 2 nm SiO_2 interlayer displayed the best photocatalytic performance due to blue-shifting in the localized

surface plasmon resonance (LSPR) and coupling energy from Ag to TiO_2 bandgap. Thicker SiO_2 interlayers decreased the photocatalytic activity because they reduced the penetration depth of the LSPR electromagnetic field into the SiO_2 layer.

Few layer ALD was also employed for the photocatalytic conversion of CO_2 to CO.³¹ Dense ZnO islands with different thickness were coated via ALD onto large arrays of massively parallel, single crystalline, high-density CuO nanowires generated by thermal oxidation of high-purity copper foils. The CO yield first increased and then decreased with increasing ALD cycles, and CuO nanowires with eight ALD cycles of ZnO islands (1.4 nm) displayed the optimal performance (**Figure 3B**). This behavior occurred because 1) the favorable band alignment and epitaxial matching between ALD ZnO nanoislands and CuO nanowires led to recombination-free charge transfer, 2) the surface morphology allowed gas exposure to both ZnO and CuO surfaces, and 3) surface defects on exposed ZnO islands resulted in lower quantum yields due to the trapping of transferred electrons.

The catalytic activity, selectivity, and stability of supported metal catalysts were also improved by few layer ALD.^{32–34} One of the most important catalysts is supported platinum. Platinum nanoparticles were deposited on Al_2O_3 by ALD (one or five

cycles) with H_2 or O_2 as the second half-cycle precursor for oxidative dehydrogenation of propane. Using H_2 as the second precursor resulted in smaller Pt particles with lower average coordination numbers than O_2 . After one ALD cycle (1.1 nm, measured by TEM), Pt catalyst with H_2 as the second precursor exhibited the highest C_3H_6 selectivity (37% at 14% conversion at 400 °C), likely due to the small particle size (**Figure 3C**). Commercial Pt catalysts (3.9 nm, measured by TEM) had a selectivity of less than 1% at 9% conversion under the same reaction conditions.³²

TiO_2 overcoated Co/ TiO_2 catalysts were also prepared to replace precious-metal catalysts, like Pt and Ru, for aqueous-phase hydrogenation (APH) reactions.³⁵ Generally, base metals (like cobalt) are inexpensive, abundant, and active for liquid phase reactions, but they have low stability caused by irreversible deactivation. **Figure 3D** shows that a thin ALD TiO_2 coating prevented both leaching and sintering of Co particles during aqueous-phase reactions, due to TiO_2 decoration of under-coordinated cobalt sites located at defects, corners, and edges. The regenerated $\text{TiO}_2/\text{Co}/\text{TiO}_2$ catalysts (30 ALD cycles, 1.2 nm) displayed much higher catalytic reactivity and stability than fresh catalysts for APH of furfuryl alcohol because more Co active sites were exposed after regeneration.³⁵

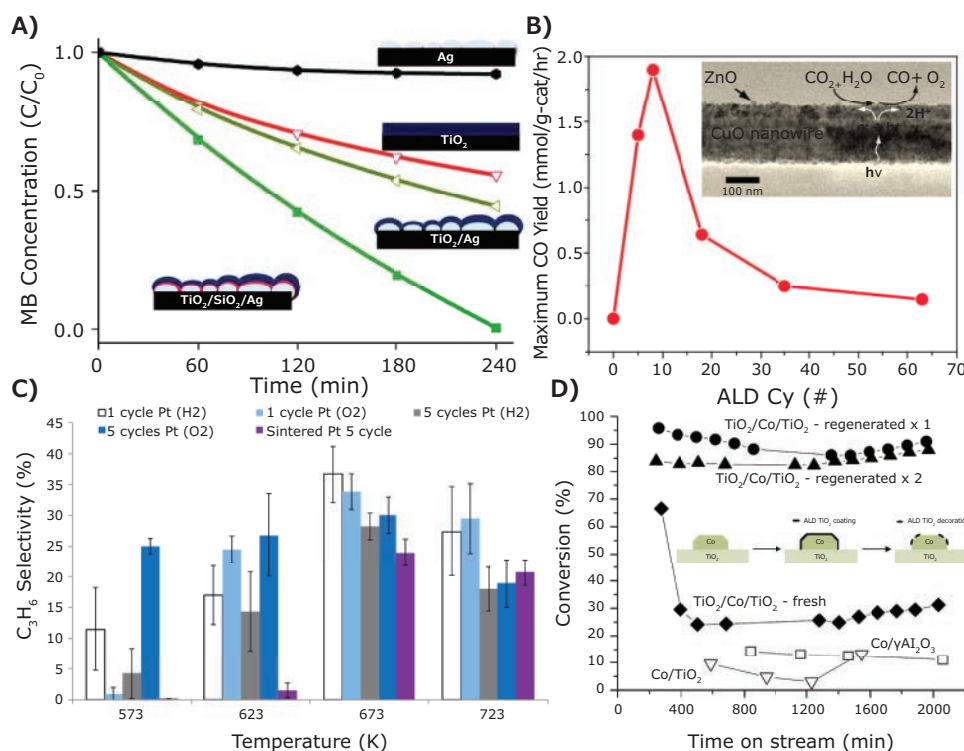


Figure 3. A) Fast decay in methylene blue from $\text{TiO}_2/\text{SiO}_2/\text{Ag}$ with 2 nm SiO_2 separation layer (green decay curve). Reproduced with permission from reference 30, copyright 2011 American Chemical Society. B) ZnO islands on CuO nanowire have optimal size (1.4 nm) for maximal $\text{CO}_2 \rightarrow \text{CO}$ conversion. Reproduced with permission from reference 31, copyright 2015 American Chemical Society. C) Pt nanoparticle catalyst (1.1 nm) using H_2 as reactant shows highest selectivity to oxidative dehydrogenation to propane at 400 °C. Reproduced with permission from reference 32, copyright 2015 American Chemical Society. D) 1.2 nm TiO_2 on Co on TiO_2 showed highest activity and stability for aqueous phase hydrogenation reactions. Reproduced with permission from reference 35, copyright 2014 Royal Society of Chemistry.

Conclusions

In summary, ALD is a singularly powerful technique that can be applied to tailor surfaces and interfaces using few monolayer films, which have a significant impact on heterogeneous material and device performance. The structure of the few monolayers can be precisely engineered, depending on how the precursor molecule interacts with the chemisorbed ligands on the substrate. If the deposition is layer-by-layer, conformal films are produced that are ideal for charge blocking or for providing surface passivation and protection. ALD films using these methods have been applied in a number of photovoltaics and batteries. On the other hand, if the ALD chemistry is driven by island nucleation followed by growth, then surfaces and interfaces can be decorated with nanocrystals in order to store charge and present chemically active facets useful for inducing chemical reactions. Their diversity in tailoring surfaces and interfaces is unique to ALD processes.

As ALD processes continue to develop, new precursor molecules are needed to provide greater flexibility for tailoring surfaces and interfaces. The interaction of precursor ligands with substrate functional groups controls nucleation of ALD films at cycle 'one'. However, it is only now becoming clear that the interaction of nearest-neighbor adsorbed precursor molecules can affect film composition, structure, and thus properties.^{36–43} This raises the interesting question as to whether the design of precursor molecules with appropriate ligand chemistry can be exploited to deterministically control film nucleation and growth on any surface.

Regardless of the application, ALD at its ultimate thickness limit has heralded a new era of surface and interface engineering. The control of this process appears to be remarkably simple, and yet has hidden complexities that will continue to push the boundaries of discovery of new materials and concept devices, and allow even finer control over their properties and applications.

Acknowledgements

The authors acknowledge financial and material support from EMD Performance Materials. Helpful discussions with Dr. Ravi Kanjolia, Dr. Charles Dezelah and Dr. Jacob Woodruff are acknowledged. Partial funding was provided by U.S. Army RDECOM Acquisition Grant W911NF-15-1-0178, Subgrant RSC15032. Partial funding was also provided through the U.S.-India Partnership to Advance Clean Energy-Research (PACE-R) for the Solar Energy Research Institute for India and the United States (SERIUS), funded by the U.S. Department of Energy (Office of Science, Office of Basic Energy Sciences, and Energy Efficiency and Renewable Energy, Solar Energy Technology Program, under subcontract DE-AC36-08GO28308 to the national Renewable Energy Laboratory, Golden, Colorado).

References

- (1) George, S. M. *Chem. Rev.* **2010**, *110*, 111–131.
- (2) Banerjee, P.; Perez, I.; Henn-Lecordier, L.; Lee, S. B.; Rubloff, G. W. *Nat. Nanotechnol.* **2009**, *4*, 292–296.
- (3) Bielski, A. R.; Boban, B.; He, Y.; Kazyak, E.; Lee, D. H.; Wang, C. M.; Tuteja, A.; Dasgupta, N. P. *ACS Nano* **2017**, *11*, 478–489.
- (4) Banerjee, P.; Lee, W.-J.; Bae, K.-R.; Lee, S. B.; Rubloff, G. W. *J. Appl. Phys.* **2010**, *108*, 043504.
- (5) Gao, Z.; Myung, Y.; Huang, X.; Kanjolia, R.; Park, J.; Mishra, R.; Banerjee, P. *Adv. Mater. Interf.* **2017**, *3*, 1600496.
- (6) Groner, M. D.; Fabreguette, F. H.; Elam, J. W.; George, S. M. *Chem. Mater.* **2004**, *16*, 639–645.
- (7) Parsons, G. N.; Atanasov, S. E.; Dandley, E. C.; Devine, C. K.; Gong, B.; Jur, J. S.; Lee, K.; Oldham, C. J.; Peng, Q.; Spagnola, J. C.; Williams, P. S. *Coord. Chem. Rev.* **2013**, *257*, 3323–3331.
- (8) Knez, M.; Kadri, A.; Wege, C.; Gösele, U.; Jeske, H.; Nielsch, K. *Nano Lett.* **2006**, *6*, 1172–1177.
- (9) Knez, M.; Niesch, K.; Niinisto, L. *Adv. Mater.* **2007**, *19*, 3425–3438.
- (10) Kim, H.; Lee, H.-B.-R.; Maeng, W. J. *Thin Solid Films* **2009**, *517*, 2563–2580.
- (11) Parsons, G. N.; George, S. M.; Knez, M. *MRS Bull.* **2011**, *36*, 865–871.
- (12) Elam, J. W.; Dasgupta, N. P.; Prinz, F. B. *MRS Bull.* **2011**, *36*, 899–906.
- (13) Johnson, R. W.; Hultqvist, A.; Bent, S. F. *Mater. Today* **2014**, *17*, 236–246.
- (14) O'Neill, B. J.; Jackson, D. H. K.; Lee, J.; Canlas, C.; Stair, P. C.; Marshall, C. L.; Elam, J. W.; Kuech, T. F.; Dumesic, J. A.; Huber, G. W. *ACS Catal.* **2015**, *5*, 1804–1825.
- (15) Dasgupta, N. P.; Lee, H.-B.-R.; Bent, S. F.; Weiss, P. S. *Chem. Mater.* **2016**, *28*, 1943–1947.
- (16) Dasgupta, N. P.; Li, L.; Sun, X. *Adv. Mater. Interfaces* **2016**, *3*, 1600914.
- (17) Meng, X.; Wang, X.; Geng, D.; Ozgit-Akgun, C.; Schneider, N.; Elam, J. W. *Mater. Horizons* **2017**, *4*, 133–154.
- (18) Chandiran, A. K.; Yella, A.; Mayer, M. T.; Gao, P.; Nazeeruddin, M. K.; Grätzel, M. *Adv. Mater.* **2014**, *26*, 4309–4312.
- (19) Park, K.; Zhang, Q.; Garcia, B. B.; Zhou, X.; Jeong, Y.-H.; Cao, G. *Adv. Mater.* **2010**, *22*, 2329–2332.
- (20) Shanmugam, M.; Baroughi, M. F.; Galipeau, D. *Thin Solid Films* **2010**, *518*, 2678–2682.
- (21) Chandiran, A. K.; Tetreault, N.; Humphry-Baker, R.; Kessler, F.; Baranoff, E.; Yi, C.; Nazeeruddin, M. K.; Grätzel, M. *Nano Lett.* **2012**, *12*, 3941–3947.
- (22) Alibabaei, L.; Farnum, B. H.; Kalanyan, B.; Brennaman, M. K.; Losego, M. D.; Parsons, G. N.; Meyer, T. J. *Nano Lett.* **2014**, *14*, 3255–3261.
- (23) Xiu, L.; Kehan, Y.; Ganhua, L.; Junhong, C.; Chris, Y. J. *Phys. D* **2013**, *46*, 024004.
- (24) Dong, X.; Fang, X.; Lv, M.; Lin, B.; Zhang, S.; Ding, J.; Yuan, N. J. *Mater. Chem. A* **2015**, *3*, 5360–5367.
- (25) Scott, I. D.; Jung, Y. S.; Cavanagh, A. S.; Yan, Y.; Dillon, A. C.; George, S. M.; Lee, S.-H. *Nano Lett.* **2011**, *11*, 414–418.
- (26) Hu, T.; Xie, M.; Zhong, J.; Sun, H.-T.; Sun, X.; Scott, S.; George, S. M.; Liu, C.-S.; Lian, J. *Carbon* **2014**, *76*, 141–147.
- (27) Yu, M.; Yuan, W.; Li, C.; Hong, J.-D.; Shi, G. J. *Mater. Chem. A* **2014**, *2*, 7360–7366.
- (28) Jung, Y. S.; Cavanagh, A. S.; Riley, L. A.; Kang, S.-H.; Dillon, A. C.; Groner, M. D.; George, S. M.; Lee, S.-H. *Adv. Mater.* **2010**, *22*, 2172–2176.
- (29) Kazyak, E.; Wood, K. N.; Dasgupta, N. P. *Chem. Mater.* **2015**, *27*, 6457–6462.
- (30) Kumar, M. K.; Krishnamoorthy, S.; Tan, L. K.; Chiam, S. Y.; Tripathy, S.; Gao, H. *ACS Catal.* **2011**, *1*, 300–308.
- (31) Wang, W.-N.; Wu, F.; Myung, Y.; Niedzwiedzki, D. M.; Im, H. S.; Park, J.; Banerjee, P.; Biswas, P. *ACS Appl. Mater. Interfaces* **2015**, *7*, 5685–5692.
- (32) Gould, T. D.; Lubers, A. M.; Corpuz, A. R.; Weimer, A. W.; Falconer, J. L.; Medlin, J. W. *ACS Catal.* **2015**, *5*, 1344–1352.
- (33) Yan, H.; Cheng, H.; Yi, H.; Lin, Y.; Yao, T.; Wang, C.; Li, J.; Wei, S.; Lu, J. J. *Am. Chem. Soc.* **2015**, *137*, 10484–10487.
- (34) Wang, H.; Wang, C.; Yan, H.; Yi, H.; Lu, J. J. *Catal.* **2015**, *324*, 59–68.
- (35) Lee, J.; Jackson, D. H. K.; Li, T.; Winans, R. E.; Dumesic, J. A.; Kuech, T. F.; Huber, G. W. *Energy Environ. Sci.* **2014**, *7*, 1657–1660.
- (36) Shi, L.; Gao, Z.; Liu, Z.; Myung, Y.; Banerjee, P. *Chem. Mater.* **2017**, *29*, 5458–5462.
- (37) Shirazi, M.; Elliott, S. D. *J. Comput. Chem.* **2014**, *35*, 244–259.
- (38) Tanskanen, J. T.; Hagglund, C.; Bent, S. F. *Chem. Mater.* **2014**, *26*, 2795.
- (39) Shirazi, M.; Elliott, S. D. *Nanoscale* **2015**, *7*, 6311–6318.
- (40) Weckman, T.; Laasonen, K. *Phys. Chem. Chem. Phys.* **2015**, *17*, 17322–17334.
- (41) Maimaiti, Y.; Elliott, S. D. *Chem. Mater.* **2016**, *28*, 6282–6295.
- (42) Goehry, C.; Schneider, N. J. *Phys. Chem. C* **2017**, *121*, 5871–5881.
- (43) Guerra-Núñez, C.; Döbeli, M.; Michler, J.; Utke, I. *Chem. Mater.* **2017**, *29*, 8690–8703.

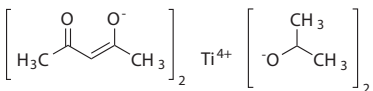
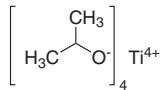
Titania Nanomaterials for Support

For a complete list of available materials, visit [SigmaAldrich.com/titaniasupport](https://sigmaaldrich.com/titaniasupport).

Name	Particle Size	Purity	Form	Cat. No.
Titanium	particle size <100 nm	98.5% trace metals basis	dispersion nanoparticles	513415-5G
Titania paste, active opaque	avg. part. size 20 nm (active) avg. part. size ≤450 nm (scatter)	-	paste (cream)	791555-5G 791555-20G
Titania paste, reflector	avg. part. size 150–250 nm (scatter)	-	paste (white)	791539-5G 791539-20G
Titania paste, transparent	avg. part. size 20 nm (active)	-	paste (yellow)	791547-10G 791547-20G
Titanium dioxide	particle size 22–25 nm (BET) 22 nm	>95% (anatase (XRD))	paste (nanocrystalline colloid)	798495-25G
	particle size 18–20 nm (BET) 18 nm	-	paste (nanocrystalline colloid)	798509-25G
	particle size 22 nm & >150 nm (BET)	-	paste (nanocrystalline colloid)	798517-25G
	particle size 18–20 nm (BET) 18 nm	>95% (anatase(XRD))	paste (nanocrystalline colloid)	798525-25G
Titanium(IV) oxide	primary particle size 21 nm (TEM)	≥99.5% trace metals basis	nanopowder	718467-100G
Titanium(IV) oxide, anatase	particle size <25 nm	99.7% trace metals basis	nanopowder	637254-50G 637254-100G 637254-500G
Titanium(IV) oxide, rutile	particle size <100 nm	99.5% trace metals basis	nanopowder, diam. × L ~10 × ~40 nm	637262-25G 637262-100G 637262-500G
Titanium(IV) oxide, mixture of rutile and anatase	particle size <50 nm (XRD) particle size <100 nm (BET)	99.5% trace metals basis	nanopowder	634662-25G 634662-100G
	particle size <250 nm (DLS) particle size ~21 nm (primary particle size of starting nanopowder)	99.9% trace metals basis	nanoparticle paste	700355-25G
	particle size ~21 nm (primary particle size of starting nanopowder) particle size <150 nm (volume distribution, DLS)	99.5% trace metals basis	dispersion nanoparticles	700347-25G 700347-100G
	particle size <100 nm particle size ~30 nm (primary particle size of starting nanopowder)	99.9% trace metals basis	dispersion nanoparticles	700339-100G

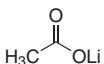
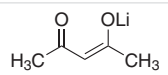
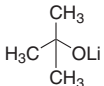
Titania Precursors for Solar Cells

For a complete list of available materials, visit [SigmaAldrich.com/solutiondeposition](https://sigmaaldrich.com/solutiondeposition).

Name	Structure	Purity (%) Or Grade	Form	Cat. No.
Titanium diisopropoxide bis(acetylacetonate)		-	solution	325252-100ML 325252-500ML
Titanium(IV) isopropoxide		99.999% trace metals basis	liquid	377996-5ML 377996-25ML 377996-100ML
		97%	liquid	205273-4X25ML 205273-100ML 205273-500ML 205273-1L 205273-2L 205273-2.5L

Lithium Precursors for Energy

For a complete list of available materials, visit [SigmaAldrich.com/solutiondeposition](https://sigmaaldrich.com/solutiondeposition).

Name	Structure	Purity (%) Or Grade	Form	Cat. No.
Lithium acetate		99.95% trace metals basis	powder or crystals	517992-100G
Lithium acetylacetonate		97%	solid	413046-25G
Lithium <i>tert</i> -butoxide		97%	powder and chunks	400173-25G 400173-100G

Name	Structure	Purity (%) Or Grade	Form	Cat. No.
Lithium <i>tert</i> -butoxide solution		-	liquid	398209-50ML 398209-250ML
Lithium ethoxide	$\text{CH}_3\text{CH}_2\text{OLi}$	95%	powder and chunks	400203-5G
Lithium ethoxide solution	$\text{CH}_3\text{CH}_2\text{OLi}$	-	liquid	400254-100ML
Lithium isopropoxide		95%	powder and chunks	348937-25G
Lithium methoxide	CH_3OLi	98%	powder	344370-25G 344370-100G
Lithium methoxide solution	CH_3OLi	-	liquid	408794-100ML 408794-800ML
Lithium phenoxide solution		-	liquid	400378-100ML
Lithium thiophenolate solution		-	liquid	400270-100ML 400270-800ML

Zinc Precursors for Catalysis

For a complete list of available materials, visit SigmaAldrich.com/solutiondeposition.

Name	Structure	Purity (%) Or Grade	Form	Cat. No.
Zinc acetate dihydrate		99.999% trace metals basis	powder or chunks	379786-5G 379786-25G
Zinc acetylacetonate hydrate		99.995% trace metals basis	solid	480991-5G 480991-25G
Zinc hexafluoroacetylacetonate dihydrate		98%	solid	132306-100G 132306-500G
Zinc trifluoroacetate hydrate		-	powder	417858-1G 394017-5G

subscribe today

Don't miss another topically focused technical review.

It's **free** to sign up for a print or digital subscription of *Material Matters*™.

- Advances in cutting-edge materials
- Technical reviews on emerging technology from leading scientists
- Peer-recommended materials with application notes
- Product and service recommendations

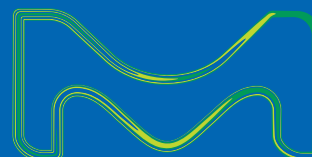


MERCK

To view the library of past issues or to subscribe, visit SigmaAldrich.com/materialmatters.

Biomaterials for Mechanoregeneration

Dr. David Mooney
Named 2018 Materials Research Society
Mid-Career Researcher



Mechanical cues regulate many aspects of biology, and we are developing materials capable of providing defined mechanical input to cells and tissues. Relevant signals include both resistance to cell intrinsic mechanical forces and application of extrinsic forces. These biomaterials can enhance the effectiveness of stem cell therapies, directly support and regenerate damaged tissues, and have led to bio-inspired new medical adhesives with unprecedented properties.

About David Mooney

David Mooney is the Pinkas Family Professor of Bioengineering in the Harvard School of Engineering and Applied Sciences, and a Core Faculty Member of the Wyss Institute. His laboratory designs biomaterials to make cell and protein therapies effective and practical approaches to treat disease. He is a member of the National Academy of Engineering, the National Academy of Medicine, and the National Academy of Inventors. He has won numerous awards, including the Clemson Award from the SFB, MERIT award from the NIH, Distinguished Scientist Award from the IADR, Phi Beta Kappa Prize for Excellence in Undergraduate Teaching, and the Everett Mendelsohn Excellence in Mentoring Award from Harvard College. His inventions have been licensed by numerous companies, leading to commercialized products, and he is active on industrial scientific advisory boards.

The life science business of Merck operates as
MilliporeSigma in the U.S. and Canada.